Redox Biology 19 (2018) 412–428

Contents lists available at ScienceDirect

Redox Biology

journal homepage: www.elsevier.com/locate/redox

Research Paper

Myostatin knockout induces apoptosis in human cervical cancer cells via elevated reactive oxygen species generation

Ying-Qian Han[a,1], Sheng-Li Ming[a,1], Hong-Tao Wu[a,1], Lei Zeng[a], Gen Ba[a], Jian Li[a], Wei-Fei Lu[a,b], Jie Han[c], Qia-Jun Du[d], Miao-Miao Sun[e], Guo-Yu Yang[a,*], Jiang Wang[a,*], Bei-Bei Chu[a,*]

[a] College of Animal Sciences and Veterinary Medicine, Henan Agricultural University, Zhengzhou, Henan Province, PR China
[b] Department of Radiology, University of Michigan, Ann Arbor, MI 48109-2200, USA
[c] Department of Endocrinology, the First Hospital of Lanzhou University, Lanzhou, Gansu Province, PR China
[d] Clinical Laboratory, the Second Hospital of Lanzhou University, Lanzhou, Gansu Province, PR China
[e] The Pathology Department of the Affiliated Cancer Hospital, Zhengzhou University, Zhengzhou, Henan Province, PR China

ARTICLE INFO

Keywords:
Myostatin
CRISPR/Cas9
Apoptosis
Reactive oxygen species

ABSTRACT

Myostatin (Mstn) is postulated to be a key determinant of muscle loss and cachexia in cancer. However, no experimental evidence supports a role for Mstn in cancer, particularly in regulating the survival and growth of cancer cells. In this study, we showed that the expression of Mstn was significantly increased in different tumor tissues and human cancer cells. Mstn knockdown inhibited the proliferation of cancer cells. A knockout (KO) of Mstn created by clustered regularly interspaced short palindromic repeats (CRISPR)/CRISPR-associated protein (Cas) 9 (CRISPR/Cas9) induced mitochondria-dependent apoptosis in HeLa cells. Furthermore, KO of Mstn reduced the lipid content. Molecular analyses demonstrated that the expression levels of fatty acid oxidation-related genes were upregulated and then increased rate of fatty acid oxidation. Mstn deficiency-induced apoptosis took place along with generation of reactive oxygen species (ROS) and elevated fatty acid oxidation, which may play a role in triggering mitochondrial membrane depolarization, the release of cytochrome c (Cyt-c), and caspase activation. Importantly, apoptosis induced by Mstn KO was partially rescued by antioxidants and etomoxir, thereby suggesting that the increased level of ROS was functionally involved in mediating apoptosis. Overall, our findings demonstrate a novel function of Mstn in regulating mitochondrial metabolism and apoptosis within cancer cells. Hence, inhibiting the production and function of Mstn may be an effective therapeutic intervention during cancer progression and muscle loss in cachexia.

1. Introduction

Mstn is a member of the transforming growth factor beta (TGF-β) superfamily and it plays an essential role in the negative regulation of skeletal muscle mass. Animals either lacking Mstn or treated with substances that block Mstn activity exhibit significant muscle hypertrophy. By contrast, Mstn overexpression or its systemic administration has been implicated in several forms of muscle loss, including severe cachexia [1,2]. Recent evidence suggests that Mstn and Activin A (another TGF-β superfamily member, shared the same receptor with Mstn to inhibit growth of muscle mass) might contribute to cancer cachexia [3–5]. Moreover, the inactivation of Mstn by treatment with an activin receptor type IIB (ActRIIB) antagonist or with an antibody directed against Mstn ablates the symptoms of cancer cachexia in tumor-bearing mice [6,7]. Therefore, Mstn appears to be critical for the pathophysiology of muscle loss during cancer progression, although the functional importance of Mstn in regulating the survival and growth of cancer cells remains obscure.

It has been shown that Mstn plays a crucial role in the regulation of lipid metabolism and energy homeostasis, where $Mstn^{-/-}$ mice exhibit suppressed body fat accumulation [8]. Furthermore, Burgess et al. observed that $Mstn^{-/-}$ mice were protected from the side effects of consuming high-fat diets, where the mice displayed reduced weight gain and intramuscular fat deposits [9]. $Mstn^{-/-}$ mice also exhibited a significant increase in energy expenditure compared with wild-type mice, which was calculated by measuring the food intake, body composition, and rates of oxygen consumption [10]. Using mouse embryonic fibroblasts isolated from Mstn-deficient and wild-type embryos, it was

* Corresponding authors.
E-mail addresses: haubiochem@163.com (G.-Y. Yang), wangjiang_hau@126.com (J. Wang), chubeibei_hau@hotmail.com (B.-B. Chu).
[1] These authors contributed equally to this work.

https://doi.org/10.1016/j.redox.2018.09.009
Received 2 August 2018; Received in revised form 20 August 2018; Accepted 12 September 2018
Available online 13 September 2018

demonstrated that a group of Mstn KO mice exhibited significantly increased levels of genes and proteins involved with energy expenditure under specialized adipogenic conditions, thereby suggesting a possible role of Mstn in the control of energy expenditure in addition to an effect on muscle mass.

Cancer cells have altered metabolic requirements compared with their normal counterparts, which are characterized by an increase in glycolysis (the Warburg effect) as well as an increased rate of glucose transport, diminished pyruvate oxidation and increased lactic acid production, increased fatty acid turnover, and a reduced fatty acid oxidation rate [11–13]. Cancer cells may be more sensitive to oxidative stress due to the high endogenous ROS levels produced by increased metabolic stress and proliferative capacity [14,15]. The reliance on increased aerobic glycolysis and reduced mitochondrial respiration can reduce ROS production, which is thought to minimize oxidative stress during the phases of high biosynthetic activity and DNA replication [16]. Furthermore, it has been reported that the increased fatty acid uptake as well as the concomitant rise in oxidative stress initiate apoptosis in cancer cells, possibly providing a selective mechanism for inducing tumor cell death [17].

In the current study, we determined the expression of Mstn in various types of tumor tissues and cancer cells, and aimed to define the mechanisms of Mstn disruption-induced growth inhibition and apoptosis in HeLa cells by using the CRISPR/Cas9 system. Our results show that Mstn is expressed in different types of tumor tissues and cancer cells. In addition, we identify a mechanistic link between cancer metabolism and growth control, which can be useful for designing novel therapeutics to treat human cancer.

2. Materials and methods

2.1. Materials

To estimate the expression of Mstn, gastric (n = 10), lung (n = 10), esophagus (n = 10) carcinoma tissues and their corresponding pericarcinous tissues (n = 10 each) were collected from Henan provincial the pathology department of the Affiliated Cancer Hospital, Zhengzhou University. This study was approved by the Research Ethics Committee of Henan provincial the Affiliated Cancer Hospital, Zhengzhou University. All these retrospective specimens were handled and made anonymous according to the ethical and legal standards. Written informed consent was obtained from all of the patients.

We obtained a CRISPR/Cas9 genome editing plasmid px330 from Addgene (42230); SYBR Premix Ex Taq (RR420A) and Trizol Reagent (D9108B) from TaKaRa Bio Inc; anti-BCL-2 antibody (#2870), anti-BAX antibody (#5023), anti-cleaved caspase-3 antibody (#9664), anti-cleaved caspase-7 antibody (#8438), anti-Mstn antibody (#MAB788), and horseradish-peroxidase-conjugated donkey anti-mouse (715-035-150) and anti-rabbit IgG (711-035-152) antibodies from Jackson ImmunoResearch Laboratories; Genomic DNA Isolation Kit (SK8221) from Sangon Biotech, Shanghai; FITC Annexin V/Dead Cell Apoptosis Kit from Invitrogen (V13242); Caspase-Glo 3/7 Assay from Promega (G8090); JC-1 probe and anti-cytochrome c antibody (AC908) from Beyotime Institute of Biotechnology (China); BODIPY493/503 from ThermoFisher; Cellular total cholesterol and triglyceride extraction kits from Applygen (China); BCA protein assay kit from DingGuo (China); N-acetylcysteine (NAC), PEG-SOD, apocynin, rhodamine 123, MitoPY1, dihydroethidium (DHE), tetramethylrhodamine methyl ester perchlorate (TMRM), from Sigma-Aldrich; and a TdT-mediated dUTP nick-end labeling (TUNEL) staining kit and dichlorofluorescein diacetate (DCFH-DA) from YEASEN Biotechnology Company (Shanghai, China); Etomoxir (CAS No.: 124083-20-1) from MedChemExpress; [9,10-^{3}H (N)]-Palmitic Acid was obtained from Perkin Elmer Life Sciences.

2.2. Cell culture

Cells were grown in monolayers at 37 °C under 5% CO_2 and maintained in Dulbecco's Modified Eagle's Medium (Gibco) containing 100 units/ml penicillin and 100 μg/ml streptomycin sulfate, which was supplemented with 10% fetal bovine serum (Gibco).

2.3. Production of Mstn-shRNA stably expressing cells

The short hairpin RNA (shRNA) sequences targeting human *Mstn* were selected using BLOCK-iT™ RNAi Designer (Life Technologies, Carlsbad, CA), i.e., sh1: GGCAGAGCATTGATGTGAAGA; sh2: GCTCTG GAGAGTGTGAATTTG; and sh3: GGTCATGATCTTGCTGTAACC. The shRNA expression cassettes against specific genes were designed as follows: forward oligo: 5′-CCGG-21bp sense-CTCG AG-21bp antisense-TTTTTG-3′, reverse oligo: 5′-AATTCAAAAA-21bp sense-CTC GAG-21bp antisense-3′. The oligos containing selected shRNA sequences were flanked by sequences compatible with the sticky ends of *Eco*RI and *Age*I. Forward and reverse oligos were annealed and ligated into the pLKO.1 vector to produce a final plasmid that expressed the shRNA of interest. Lentiviral particles were then produced. Briefly, 4×10^6 human HEK293T cells were plated on 10-cm dishes at 24 h before transfecting with 1 μg shRNA containing pLKO.1 vector, 0.75 μg psPAX2 (packaging plasmid), and 0.25 μg pMD2.G (envelope plasmid). Transfection used a ratio of three volumes FuGENE® HD (μL) to one volume DNA (μg). The medium was changed after 16 h. Viral particles were collected at 48 h after transfection and used to infect human cancer cells (Huh7, HeLa, HepG2, and A549) and non-tumorigenic HEK293 cells. The infected cells were selected in culture medium containing puromycin for 2 weeks.

2.4. gRNA cloning method

The genomic target sequence (5′-CTCATCAAACCTATGAAAGA-3′) of *Mstn* for the specificity of the Cas9 nuclease immediately precedes a 5′-NGG-3′ protospacer adjacent motif (PAM). Two partially complementary oligonucleotides (5′-CACCGTCATCAAACCTATGAAAGA-3′ and 5′-AAACTCTTTCATAGGTTTG ATGAC-3′) were synthesized, annealed, and ligated into pX330 after digestion using the *Bbs*I restriction enzyme. This plasmid (designated as the *Mstn* KO plasmid) contained two expression cassettes, hSpCas9 and the chimeric guide RNA, which could guide hSpCas9 to the genomic target site in *Mstn*.

2.5. Establishment of HeLa/Mstn KO cells

HeLa cells were seeded into a 60 mm dish at a density of 5×10^5. The Mstn KO plasmid was transfected into cells with Lipofectamine 2000 (Invitrogen) according to the manufacturer's instructions. After 48 h, the cells were dissociated by trypsinization to obtain single cells. The cells were counted and serially diluted in culture medium to a final concentration of 0.5 cells per 100 μL in a 96-well plate, which was followed by an expansion period to establish a new clonal cell line. To identify the status of genome editing, PCR amplification was performed with the genomic DNA isolated from different clonal cell lines and primers specific for the target sequence, followed by DNA sequencing.

2.6. Immunoblotting analysis

Whole cell lysates were prepared with RIPA buffer supplemented with protease inhibitors (Roche). Protein samples were separated by SDS-PAGE and transferred to cellulose nitrate membranes (Whatman), after incubation in 5% nonfat milk for 1 h. The membrane was incubated with the primary antibody at 4 °C overnight and then incubated

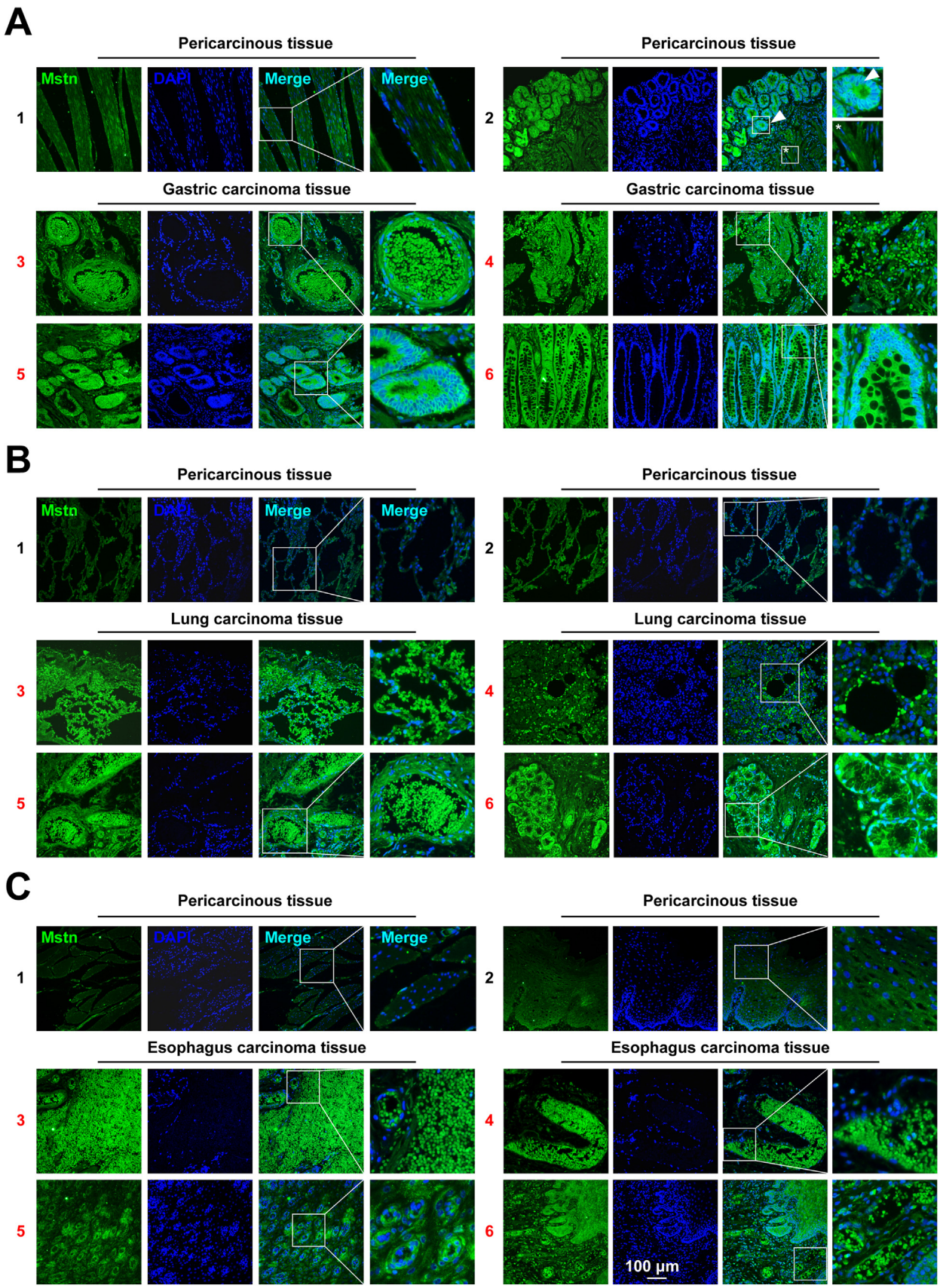

Fig. 1. The expression of Mstn was up-regulated in human gastric, lung and esophagus cancers. (A) The expression pattern of Mstn in human gastric carcinoma (3–6) and corresponding pericarcinous tissues (1–2) was determined by immunofluorescent staining. The boxed region in the left image is enlarged on the right. The arrowhead indicates cancer cells, and the asterisk (*) indicates the remaining normal cells that have not yet been cancerous. (B) The expression pattern of Mstn in human lung carcinoma (3–6) and corresponding pericarcinous tissues (1–2) was determined by immunofluorescent staining. (C) The expression pattern of Mstn in human esophagus carcinoma (3–6) and corresponding pericarcinous tissues (1–2) was determined by immunofluorescent staining. Scale bar, 100 μm.

with the horseradish-peroxidase-conjugated secondary antibody for 1 h. The target proteins were detected using Luminata™ Crescendo Western HRP Substrate (Millipore). Each experiment was repeated at least three times using separate batches of cells.

2.7. Caspase 3/7 activity analysis

The activities of caspases 3 and 7 were analyzed using the Caspase-Glo 3/7 Assay according to the manufacturer's instructions. The luminescent signals were detected using a Fluoroskan Ascent™ Microplate

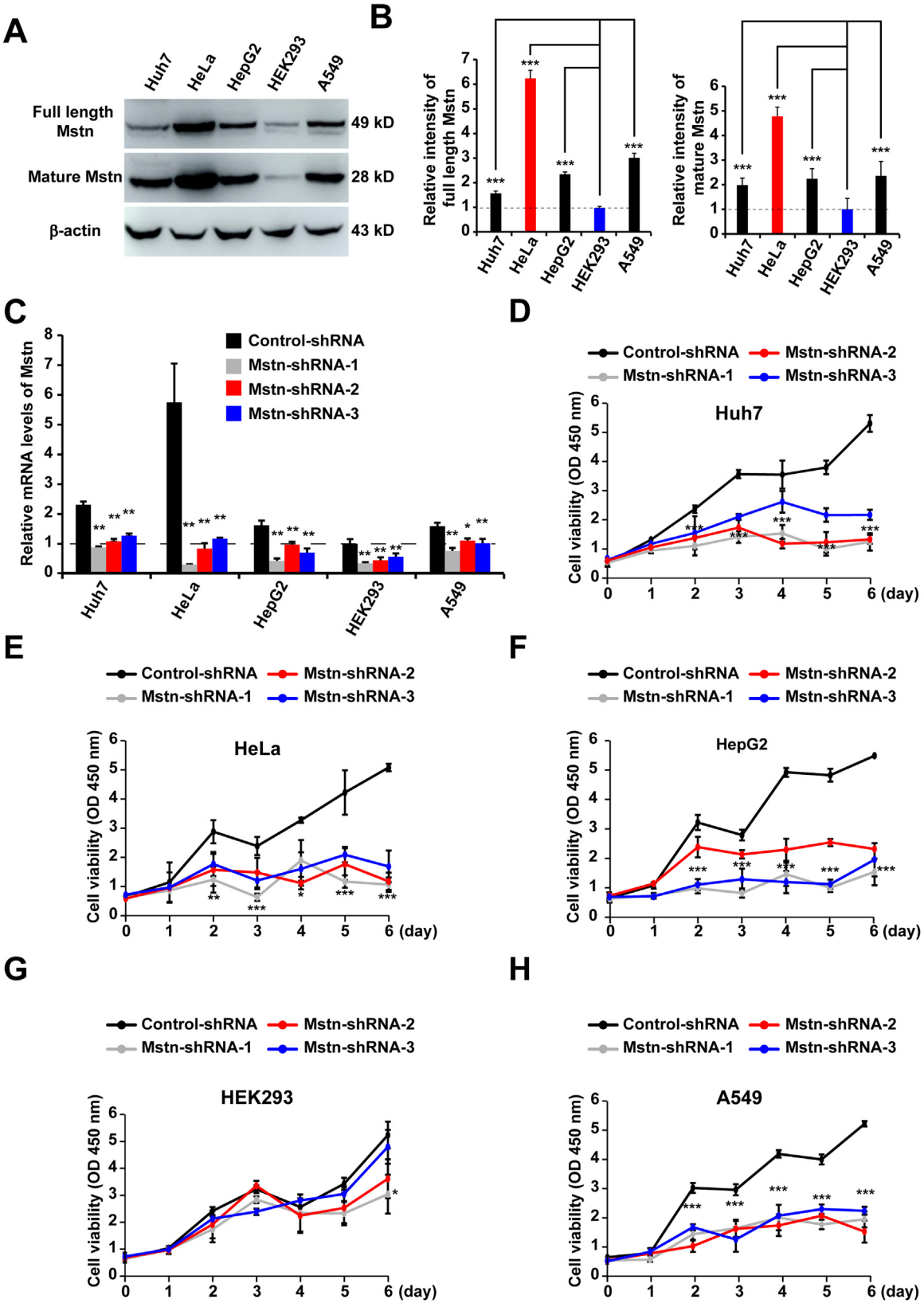

(caption on next page)

Fig. 2. Expression of Mstn in human cancer and non-tumorigenic HEK293 cells, the Mstn knockdown inhibited growth of cancer cells. (A) Immunoblot analyses of Mstn expression in human cancer (Huh7, HeLa, HepG2, and A549) and non-tumorigenic HEK293 cells. The antibodies used are indicated on the left. Each blot is representative of three independent experiments. (B) Semi-quantitative densitometric analyses of the full length Mstn and the mature Mstn shown in (A) using Image J software. The protein content was normalized against the corresponding β-actin level. Data represent the mean ± standard error of the mean based on three independent experiments, which were analyzed by one-way ANOVA. $^{***}P < 0.0001$. (C) The mRNA levels of *Mstn* in shRNAs stably expressing cells were detected by Q-PCR. Values were normalized relative to the *β-Actin* mRNA levels. Data represent the mean ± standard error of the mean based on three independent experiments. $^{*}P < 0.05$, $^{**}P < 0.01$, one-way ANOVA. (D) Proliferation of control-shRNA or Mstn-shRNAs stably expressing Huh7 cells was determined using the CCK8 assay. Data represent the mean ± standard error of the mean based on three independent experiments, which were analyzed by one-way ANOVA. $^{***}P < 0.0001$. (E) Proliferation of control-shRNA or Mstn-shRNAs stably expressing HeLa cells was determined using the CCK8 assay. Data represent the mean ± standard error of the mean based on three independent experiments, which were analyzed by one-way ANOVA. $^{*}P < 0.05$, $^{**}P < 0.01$, $^{***}P < 0.0001$. (F) Proliferation of control-shRNA or Mstn-shRNAs stably expressing HepG2 cells was determined using the CCK8 assay. Data represent the mean ± standard error of the mean based on three independent experiments, which were analyzed by one-way ANOVA. $^{***}P < 0.0001$. (G) Proliferation of control-shRNA or Mstn-shRNAs stably expressing HEK293 cells was determined using the CCK8 assay. Data represent the mean ± standard error of the mean based on three independent experiments, which were analyzed by one-way ANOVA. $^{*}P < 0.05$. (H) Proliferation of control-shRNA or Mstn-shRNAs stably expressing A549 cells was determined using the CCK8 assay. Data represent the mean ± standard error of the mean based on three independent experiments, which were analyzed by one-way ANOVA. $^{***}P < 0.0001$.

Fluorometer FL (Thermo Scientific). The results were calculated as representative examples based on three independent experiments.

2.8. Annexin V/PI Cell Apoptosis analysis

Annexin V/PI (propidium iodide) staining was performed using an FITC Annexin V/Dead Cell Apoptosis Kit according to the manufacturer's instructions. Briefly, cells were grown in a 6-well plate for 24 h, washed with PBS, and digested with Trypsin-EDTA solution. Cells were then collected by centrifugation and washed twice with ice-cold PBS. After washing one more time with 1x annexin-binding buffer, the cells were incubated in 100 μL annexin-binding buffer containing 5 μL annexin V and 1 μL PI for 15 min in the dark. Flow cytometric analysis was performed to monitor the green fluorescence of the FITC-conjugated

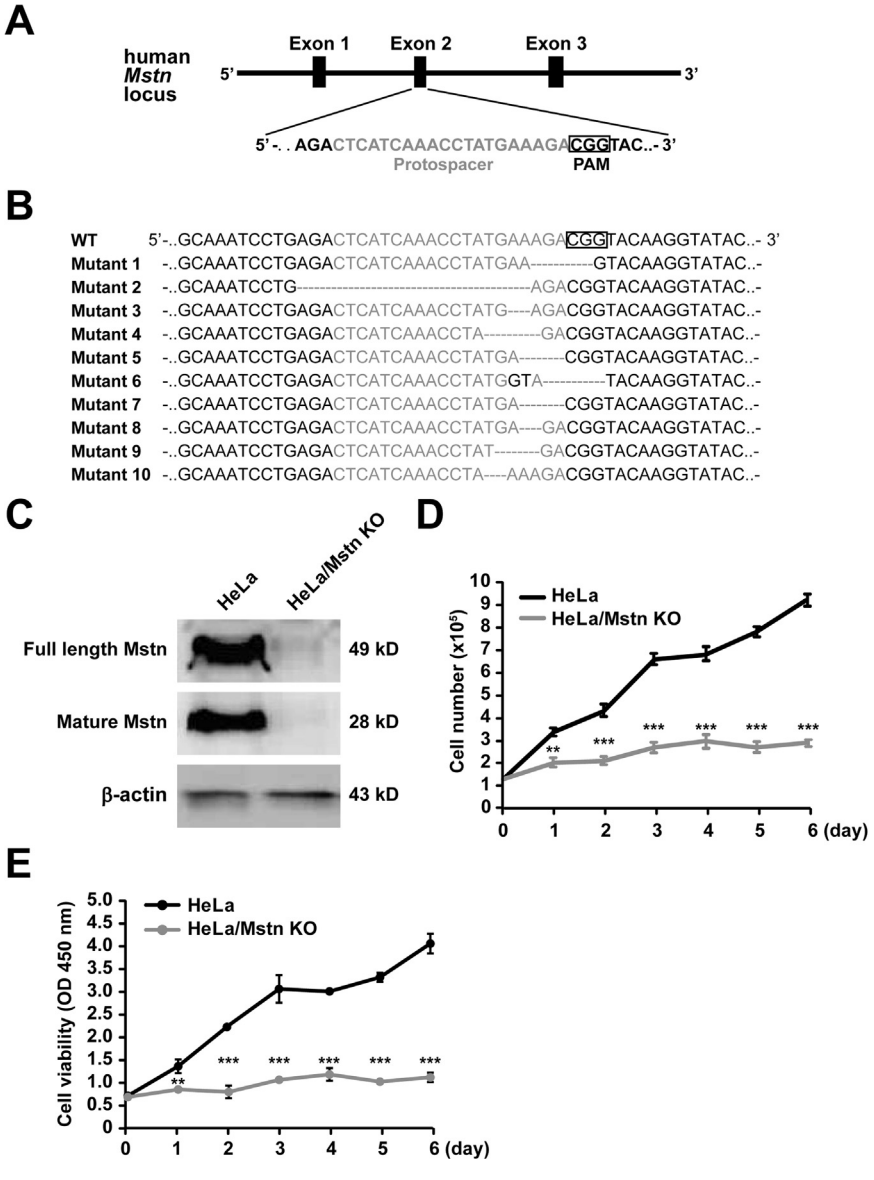

Fig. 3. Generation of HeLa/Mstn KO cells using CRISPR/Cas9. (A) Schematic diagram of sgRNA targeting the human *Mstn* exon 2 locus. Protospacer sequences are colored grey. The PAM sequence is framed by a black box. (B) Sequencing of PCR amplification products from Mstn mutant clones confirmed the introduction of insertion-deletion polymorphisms (indels) in exon 2. (C) Immunoblot analysis of Mstn expression in HeLa and HeLa/Mstn KO cells. The antibodies used are indicated on the left. (D) Time-course analysis of viable cell numbers in HeLa and HeLa/Mstn KO cells. Data represent the mean ± standard error of the mean based on three independent experiments, which were analyzed by one-way ANOVA. $^{**}P < 0.01$, $^{***}P < 0.0001$. (E) Proliferation of HeLa and HeLa/Mstn KO cells was determined using CCK8 assays. Data represent the mean ± standard error of the mean based on three independent experiments, which were analyzed by one-way ANOVA. $^{**}P < 0.01$, $^{***}P < 0.0001$.

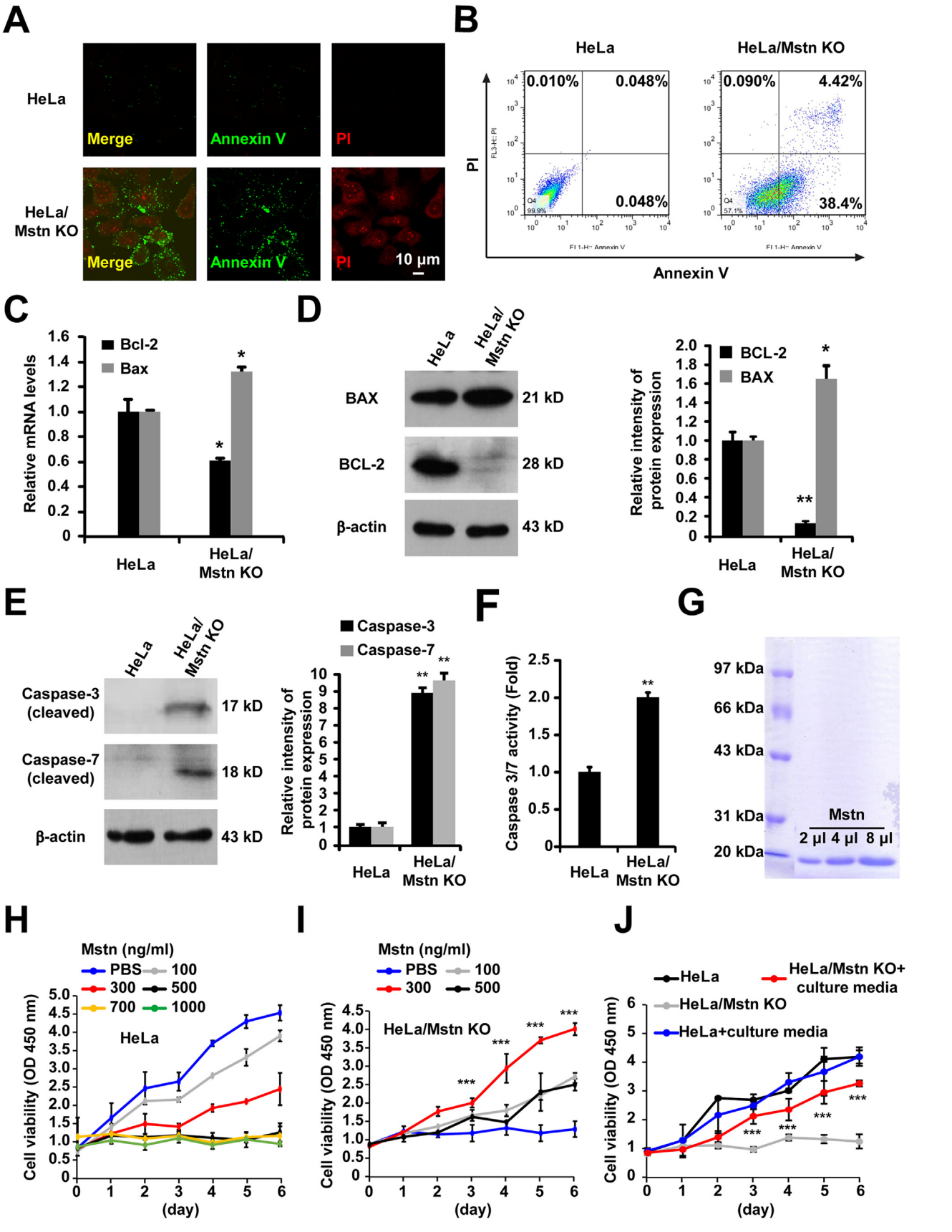

(caption on next page)

Fig. 4. Mstn KO promoted HeLa cell apoptosis. (A) Cells were co-stained with Annexin V/PI and fluorescence was detected using a fluorescence microscope. Scale bar, 10 μm. Each image is representative of three independent experiments. (B) Cells were stained with Annexin V/PI and apoptosis was determined using flow cytometry. (C) The mRNA levels of *Bcl-2* and *Bax* were detected by Q-PCR. Values were normalized relative to the *β-Actin* mRNA levels. Data represent the mean ± standard error of the mean based on three independent experiments. $^{*}P < 0.05$, unpaired two-tailed *t*-test. (D) Immunoblot analysis was performed using the indicated antibodies. Semi- quantitative densitometric analyses of BCL-2 and BAX were performed using Image J. The protein content was normalized against the corresponding β-actin content. Data represent the mean ± standard error of the mean based on three independent experiments. $^{*}P < 0.05$, $^{**}P < 0.01$. (E) Immunoblot analysis was performed with the indicated antibodies. Semi- quantitative densitometric analysis of cleaved caspase-3 and caspase-7 was performed using Image J. The protein content was normalized against the corresponding β-actin content. Data represent the mean ± standard error of the mean based on three independent experiments. $^{**}P < 0.01$. (F) The activities of caspase 3 and 7 were analyzed using the Caspase-Glo 3/7 assay. Data represent the mean ± standard error of the mean based on three independent experiments. $^{**}P < 0.01$, unpaired two-tailed *t*-test. (G) Recombinant Mstn was expressed and purified as described previously [28]. The purified recombinant Mstn (Lys193-Ser375) protein was visualized by coomassie blue staining. (H) HeLa cells were treated with PBS or Mstn at different concentrations (100, 300, 500, 700, 1000 ng/ml) for the indicated times. Proliferation of cells was determined using the CCK8 assay. Data represent the mean ± standard error of the mean based on three independent experiments. (I) HeLa/Mstn KO cells were treated with PBS or Mstn at different concentrations (100, 300, 500 ng/ml) for the indicated times. Proliferation of cells was determined using the CCK8 assay. Data represent the mean ± standard error of the mean based on three independent experiments, which were analyzed by one-way ANOVA. $^{***}P < 0.0001$. (J) Cells were treated with culture media from normal HeLa cells for the indicated times. Proliferation of cells was determined using the CCK8 assay. Data represent the mean ± standard error of the mean based on three independent experiments, which were analyzed by one-way ANOVA. $^{***}P < 0.0001$.

annexin V (488 nm) and the red fluorescence of DNA-bound PI (530 nm) using a BD AccuriC6 flow cytometer. All data were analyzed using FlowJo software.

Cells were grown on coverslips and co-stained with annexin V and PI. After washing with 1x annexin-binding buffer, cells were fixed, mounted, and the fluorescent signals were detected by confocal microscopy (Leica TCS SP5).

2.9. Tumor xenograft model and TUNEL assay

Experiments involving animals were performed in accordance with the rules approved by the State Council of the People's Republic of China for experimental animal care and use. Four-week-old female BALB/c nude (nu/nu) mice were injected in the flank regions with 4×10^6 HeLa cells in 200 μL of medium. Tumor size and body weight measurements were initiated 7 days post-inoculation and they were recorded every 4 days. Tumor dimensions were measured with calipers and the volumes calculated using the following formula: length × width^2 × 0.5. All mice were sacrificed 31 days after cell injection, and tumor tissues were collected and weighed.

Apoptotic cells in xenografts were identified by TUNEL staining using an In Situ Cell Death detection kit (TUNEL Apoptosis Detection Kit; YEASEN). The tumor tissue samples were treated according to the manufacturer's directions and examined using a fluorescent microscope. The TUNEL-positive cells were counted and the apoptosis index was calculated according to the following formula: (number of apoptotic cells/total number of nuclei) × 100%.

Four-week-old female BALB/c nude (nu/nu) mice were injected in the flank regions with 1×10^7 HeLa/Mstn KO cells in 200 μL of medium (containing PBS or Mstn at a concentration of 300 ng/ml). Seven days after implantation, animals from PBS (n = 8) or Mstn (n = 8) groups were selected to receive direct intratumoral injection of PBS or Mstn at a concentration of 0.5 mg/kg/day. Tumor sizes and body weights of mice were recorded every 4 days. Tumor dimensions were measured with calipers and the volumes calculated using the following formula: length × width^2 × 0.5. All mice were sacrificed 31 days after cell injection, and tumor tissues were collected and weighed.

2.10. Quantitative real-time PCR (Q-PCR)

Total RNA was extracted from cells with Trizol Reagent and reverse transcribed into cDNA with an oligo (dT) primer. Q-PCR was performed using an Eppendorf Mastercycler® ep realplex system according to the manufacturer's protocol. All reactions were performed in triplicate and the relative amounts of mRNAs were calculated with the comparative CT method. The results obtained were representative of three independent experiments.

2.11. Measurement of ROS production

The intracellular generation of ROS was analyzed using DCFH-DA. The non-fluorescent ester penetrated into the cells and it was hydrolyzed to DCFH by cellular esterases. The probe was rapidly oxidized to yield the highly fluorescent compound, 2′7′-dichlorofluorescein (DCF), in the presence of cellular peroxidase and ROS such as hydrogen peroxide or fatty acid peroxides [18]. Briefly, cells (1×10^6) were cultured and loaded with 10 μM DCFH-DA for 30 min at 37 °C in the dark, and then washed three times with PBS. The fluorescence was measured within 1 h at an excitation wavelength of 488 nm and an emission wavelength of 525 nm.

DHE was used to assess superoxide as a marker of oxidative stress because the membrane-permeable DHE was oxidized by superoxide anions to form ethidium (ETH), which bound to DNA and produced the fluorescent ETH-DNA [19]. Cells were incubated with 5 μM DHE for 30 min at 37 °C in the dark and then rinsed three times with PBS. Cells were visualized and counted within 1 h by fluorescence microscopy.

Mitochondria peroxy yellow 1 (MitoPY1) uses a triphenylphosphonium targeting group and a boronate-based molecular switch to selectively respond to the localized changes in mitochondrial hydrogen peroxide concentrations generated by oxidative stress conditions [20]. Cells were incubated with 5 μM MitoPY1 at 37 °C for 30 min in the dark and then rinsed three times with PBS. Cells were visualized and counted within 1 h by fluorescence microscopy.

2.12. Cell proliferation assay

The cell viability was evaluated using the CCK8 assay according to the manufacturer's instructions. In brief, cells were seeded into 96-well plates with 1×10^4 cells/well and incubated in the absence or presence of NAC, PEG-SOD, apocynin or etomoxir for specific time periods. Next, 10 μL of CCK8 was added to each well and the culture medium was incubated at 37 °C for 3 h. The absorbance was detected at 450 nm using a microplate reader (Awareness Technology Inc.).

2.13. Mitochondrial membrane potential assay

Changes in the mitochondrial membrane potential were assessed by JC-1 staining according to the manufacturer's protocol. In brief, cells grown on coverslips were stained with JC-1 dye and then observed under a fluorescence microscope. Red fluorescence indicated JC-1 aggregates (excitation/emission = 540/605 nm) formed in normal cells with high $\Delta\psi_m$, whereas green fluorescence denoted JC-1 monomers (excitation/emission = 480/510 nm) in apoptotic or unhealthy cells with low $\Delta\psi_m$ [21].

TMRM accumulates in hyperpolarized mitochondria and the fluorescence intensity correlates with $\Delta\psi_m$ [22]. Cells were incubated with

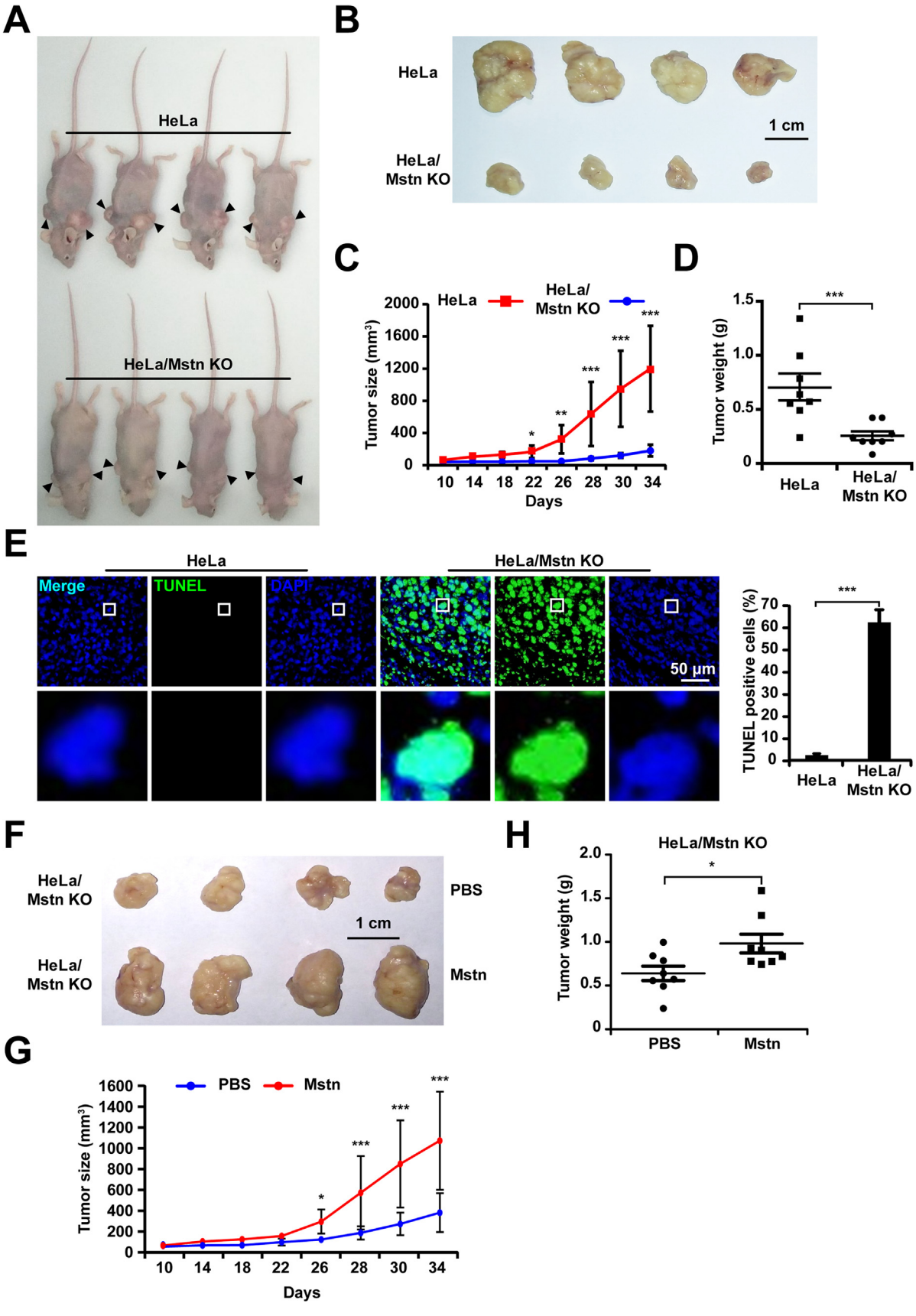

(caption on next page)

Fig. 5. Mstn KO inhibited growth of tumor xenograft in nude mice. (A) Representative mice bearing tumors after 34 days post inoculation. Black arrowheads, inoculation sites. (B) Cells were injected into nude mice and four representative xenograft tumors in each group are shown. Scale bar, 1 cm. (C) Tumor sizes were measured on the days indicated and the tumor volumes were calculated. Data represent the mean ± standard error of the mean (n = 8 per group). $^{*}P < 0.05$, $^{**}P < 0.01$, $^{***}P < 0.0001$, one-way ANOVA. (D) Tumor weights are shown in the scatter plot. Data represent the mean ± standard error of the mean (n = 8 per group). $^{***}P < 0.0001$, unpaired two-tailed *t*-test. (E) Representative images of fluorescent TUNEL and DAPI staining of xenograft tumor sections. The boxed region in the image is enlarged below. Scale bar, 50 μm. The percentages of apoptotic cells in tumor xenografts were quantified and normalized versus the number of nuclei. At least 300 cells from each section were counted. Data represent the mean ± standard error of the mean. $^{***}P < 0.0001$, unpaired two-tailed *t*-test. (F) HeLa/Mstn KO cells were injected into nude mice and PBS or Mstn were injected intratumorally. Four representative xenograft tumors in each group with the treatment of PBS or Mstn were shown. Scale bar, 1 cm. (G) Tumor sizes were measured on the days indicated and the tumor volumes were calculated. Data represent the mean ± standard error of the mean (n = 8 per group). $^{*}P < 0.05$, $^{***}P < 0.0001$, one-way ANOVA. (H) Tumor weights are shown in the scatter plot. Data represent the mean ± standard error of the mean (n = 8 per group). $^{*}P < 0.05$, unpaired two-tailed *t*-test.

20 nM TMRM for 30 min at 37 °C in the dark and then rinsed three times with PBS. Cells were visualized and counted within 1 h by fluorescence microscope.

Rhodamine 123 was used to evaluate changes in the mitochondrial membrane potential [23]. Cells were incubated with 1 μM rhodamine 123 for 30 min at 37 °C in the dark and then rinsed three times with PBS. Cells were visualized and counted by fluorescence microscopy within 1 h.

2.14. Subcellular fractionation

Subcellular fractionation was performed to determine the localization of Cyt-c. In brief, cells were harvested, washed, and homogenized in 500 μL of subcellular fractionation buffer [250 mM sucrose, 20 mM HEPES (pH 7.4), 10 mM KCl, 1.5 mM $MgCl_2$, 1 mM EGTA, 1 mM EDTA, 1 mM DTT, protease and phosphatase inhibitor cocktail]. The lysates were centrifuged at 700*g* for 5 min at 4 °C to separate the nuclear fraction. Next, the supernatant containing the mitochondrial and cytoplasmic fractions was centrifuged again at 10,000*g* for 15 min at 4 °C. The resulting supernatant was used as the cytoplasmic fraction, and the pellet was washed three times with ice-cold PBS and used as the mitochondrial fraction.

2.15. Lipid droplets (LDs) staining

Cells were washed in PBS and fixed with 4% paraformaldehyde for 30 min. After washing with PBS, cells were incubated with 2 μg/ml Bodipy 493/503 (493 nm excitation/503 nm emission) in PBS for 30 min at 37 °C. Digital images were obtained with a fluorescence microscopy.

Cells were washed in PBS and fixed with 4% paraformaldehyde for 30 min. After washing with PBS, cells were stained with Oil Red O (Sigma) solution (Oil Red O saturated solution in isopropanol: water at 3:2) for 15 min. The cells were then washed with 70% alcohol for 5 s to remove background staining, rinsed in double-distilled Millipore water, counterstained with Harris hematoxylin (10 s), mounted, and observed under a light microscope. The diameters of the observed lipid droplets (LDs) were calculated by averaging multiple diameter measurements with Image J software. The LDs number was obtained by Image J analyze particles function (particle area less than 0.01 mm^2 were excluded).

2.16. Measurement of fatty acid oxidation

Fatty acid oxidation assays were carried out as described [24]. In brief, cells were incubated with MEM Alpha medium containing 5 μCi/ml [9,10-^{3}H(N)]- Palmitic Acid and 2% fatty acid free BSA overnight. After incubation, the medium was recovered and excess ^{3}H-palmitate in the medium was removed by precipitating twice with an equal volume of 10% trichloroacetic acid. The supernatants were extracted by addition of 5 ml of methanol: chloroform (2:1) twice, and an aliquot of the aqueous phase was taken for counting the content of ^3H_2O with a liquid scintillation. The values were normalized to total cellular protein content, which were determined with a BCA protein assay kit (Bio-Rad).

2.17. Statistical analysis

In the quantitative analyses, data were obtained based on at least three independent experiments and they were expressed as the mean ± standard error of the mean. Statistical analysis was performed using the *t*-test or one-way analysis of variance (ANOVA). Significant differences were accepted at $^{*}P < 0.05$, $^{**}P < 0.01$, and $^{***}P < 0.0001$ versus the corresponding controls.

3. Results

3.1. Expression of Mstn in gastric, lung, esophagus cancer and their pericarcinous tissues

Mstn plays an important role in the activation of muscle wasting during cancer cachexia [7,25]. To clarify the function of Mstn in the development of cancer, the clinical expression of Mstn in patients with gastric, lung, esophagus cancer was analyzed. Here we collected gastric (n = 10), lung (n = 10), esophagus carcinoma tissues (n = 10) and their corresponding pericarcinous tissues (n = 10 each). An immunofluorescent staining analysis using anti-Mstn and DAPI were conducted. The results showed that, compared with pericarcinous tissues, the expression of Mstn in gastric, lung and esophageal cancers was significantly increased (Fig. 1). Moreover, compared with the cells that were not yet cancerous (Fig. 1A2, *), the structure of gastric adenocarcinoma showed a more pronounced Mstn expression (Fig. 1A2, arrowhead). It is interesting to note that in all three cancers, a capsule like structure was found, which contained a large number of Mstn (Figs. 1A3, 1B5, 1C3, 1C4, 1C6). However, no positive signal was observed in the pericarcinous tissue (Figs. 1A1, 1B1, 1B2, 1C1, 1C2). These findings suggest that Mstn protein plays an important role in cancer progression.

3.2. Mstn expression in human cancer cells and its knockdown inhibited their proliferation

To investigate the function of Mstn in cachexia-inducing cancer cells, western blot analyses were performed in order to compare the Mstn expression levels in human cancer cells with those in non-tumorigenic HEK293 cells. As illustrated in Fig. 2A, human cancer cell lines from different tissue sources such as hepatocarcinoma (Huh-7), cervical cancer (HeLa), liver carcinoma (HepG2), and adenocarcinoma human alveolar basal epithelial (A549) cells had significantly higher Mstn expression levels than the non-tumorigenic HEK293 cells [26,27]. β-actin was used as a loading control and we confirmed that a similar quantity of protein was loaded in each lane. The levels of both the full length and mature forms of Mstn were highest in HeLa cells (Fig. 2B). To examine whether Mstn affected cancer cell survival and growth, lentivirus-delivered shRNAs were used to stably knock down *Mstn*. All the Mstn-shRNAs transfected cells exhibited significant reductions in their *Mstn* mRNA levels compared with the control-shRNA cells (Fig. 2C). *Mstn* knockdown dramatically inhibited the proliferation of cancer cells compared with HEK293 cells (Figs. 2D–2H). These results indicated that lentivirus-mediated Mstn knockdown inhibited the

growth of cancer cells, but it had little effect on the non-tumorigenic HEK293 cells. Among these cancer cells, HeLa had the highest full length and mature forms of the Mstn expression levels, so we selected this cell line for further characterization.

3.3. CRISPR/Cas9-mediated Mstn KO in HeLa cells

To further confirm the effects of Mstn disruption on cancer cell proliferation, CRISPR/Cas9 was used to knock out Mstn in HeLa cells. The pX330 plasmid expressing both hSpCas9 and a sgRNA targeting

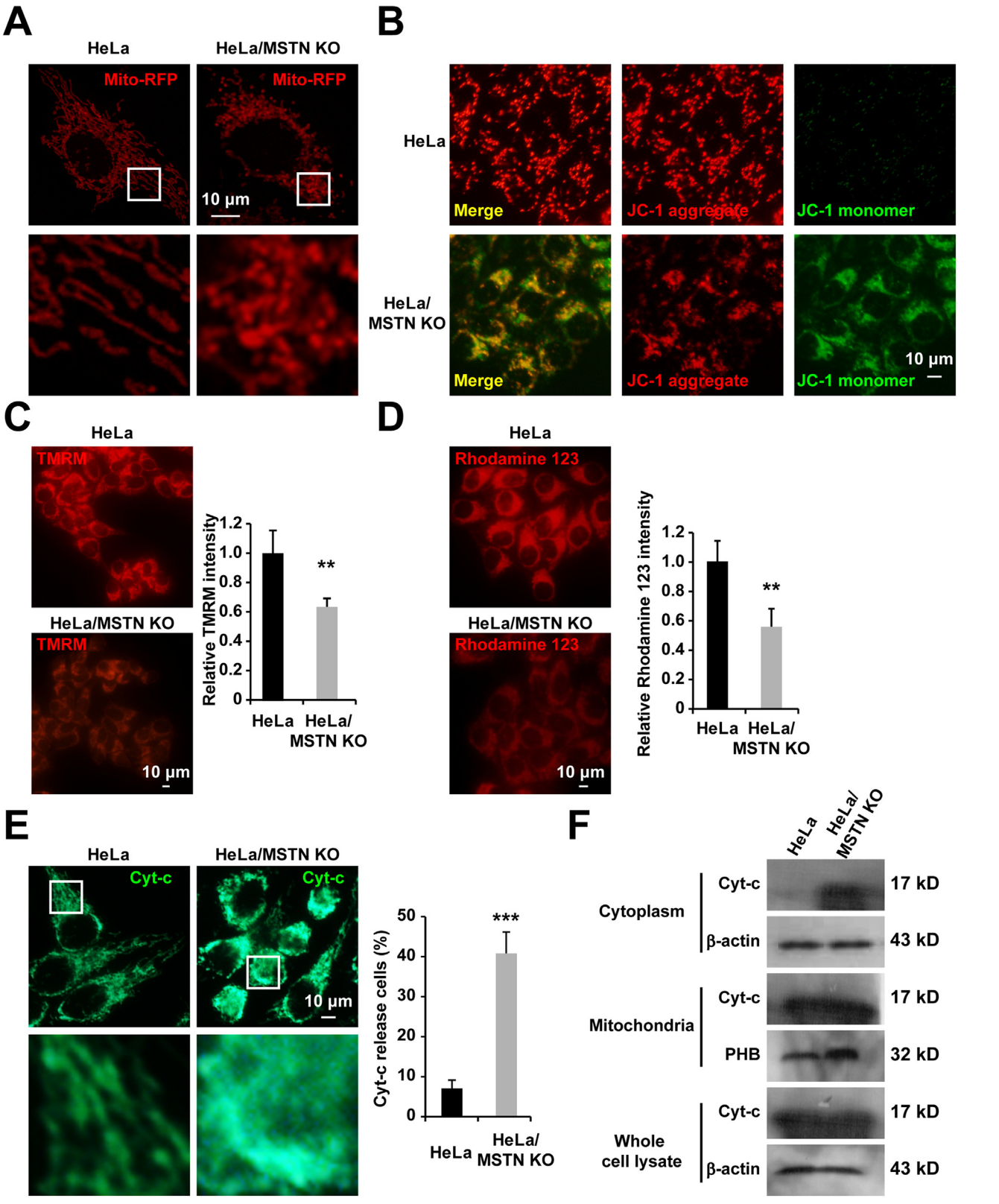

(caption on next page)

Fig. 6. Mstn KO induced mitochondrial apoptosis in HeLa cells. (A) Mstn KO altered the mitochondrial morphology in Hela cells. Cells were transiently transfected with mito-RFP for 24 h, fixed, and the mito-RFP signals were measured using confocal microscopy. Scale bar, 10 μm. Boxed region in the top image is enlarged below. Each image is representative of three independent experiments. (B) Cells were stained with JC-1 to measure the changes in the mitochondrial membrane potential and observed by fluorescence microscopy. Scale bar, 10 μm. Each image is representative of three independent experiments. (C) Representative fluorescence image of cells loaded with TMRM. Scale bar, 10 μm. Quantitative changes in the TMRM fluorescence intensity was analyzed by Image J. At least 300 cells were analyzed based on three independent experiments. Data represent the mean ± standard error of the mean. $^{**}P < 0.01$, unpaired two-tailed *t*-test. (D) Representative fluorescence image of cells loaded with rhodamine 123. Scale bar, 10 μm. Quantitative changes in the rhodamine 123 fluorescence intensity were analyzed by Image J. At least 300 cells were analyzed based on three independent experiments. Data represent the mean ± standard error of the mean. $^{**}P < 0.01$, unpaired two-tailed *t*-test. (E) Immunostaining of Cyt-c was observed by fluorescence microscopy. Scale bar, 10 μm. The percentage of cells that released Cyt-c into the cytoplasm was counted. At least 300 cells were analyzed based on three independent experiments. Data represent the mean ± standard error of the mean. $^{***}P < 0.0001$, unpaired two-tailed *t*-test. (F) The release of mitochondrial Cyt-c was estimated by examining the Cyt-c protein content of mitochondria and the extracted mitochondria-free cytoplasmic fraction by western blotting. Prohibitin (PHB) and β-actin antibodies were used as loading controls for the mitochondrial and cytoplasmic fractions, respectively. Results are representative of three independent experiments.

exon 2 of Mstn with a 5′-NGG-3′ PAM transfected in HeLa (Fig. 3A) and single cell clones were then grown up. The presence of Mstn mutations in genomic DNA was measured by DNA sequencing. Some of the clones (37%) had a nucleotide insertion/deletion near the PAM site (Fig. 3B). To assess the KO efficiency, the Mstn protein levels in different mutant clones were measured by immunoblotting (data not shown). We then selected a clone with sufficient Mstn KO. As shown in Fig. 3C, the levels of Mstn were greatly reduced in clone-9 compared with the control HeLa cells (pX330 empty plasmid). This KO was due to a four-nucleotide deletion that introduced a premature stop codon, which indicated an effective disruption (Fig. S1). To test whether off-target mutations occurred in clone-9, we first searched for nucleotide sequences in the human genome that were identical to the sgRNA but with up to three or four base pair (bp) mismatches. We predicted eight potential off-target candidate sites. These off-target sites comprising approximately 300 bp regions were then amplified and sequenced. No mutations were observed in these eight hypothetical off-target loci in clone-9 (Fig. S2). When cultured in the same conditions, the Mstn KO cells exhibited a marked decrease in their growth rate at specific time points and there were seven times more HeLa cells than KO cells on day 6 based on the number counts (Fig. 3D). Cell viability measured using the CCK8 assay also confirmed that the loss of Mstn hindered cancer cells' growth (Fig. 3E).

3.4. Mstn KO induced apoptosis in HeLa cells

We also investigated the possibility that Mstn KO reduced growth of HeLa cells by increasing apoptosis. Apoptosis was analyzed using Annexin V-FITC and PI double staining by confocal microscopy and flow cytometry. The results showed that Mstn KO induced phosphatidylserine externalization to the outer leaflet of the plasma membrane. PI cannot permeate live cells and observations of PI positivity in the Mstn KO cells confirmed the presence of apoptosis (Fig. 4A). As shown in Fig. 4B, the percentage of apoptotic cells significantly increased in the Mstn KO group compared with that in the control group (42.82% vs. 0.098%) ($P < 0.0001$). Q-PCR and western blot detected elevated Bax levels but also a reduction in the expression of Bcl-2 due to the Mstn KO (Figs. 4C, 4D). Moreover, profound cleavage of caspase-3 and caspase-7 were also observed (Fig. 4E). We also found that the caspase activity was markedly enhanced in HeLa/Mstn KO cells using the Caspase-Glo 3/7 assay ($P < 0.01$) (Fig. 4F). Furthermore, the lentivirus-mediated knockdown of Mstn in human cancer cells (Huh-7, HeLa, HepG2, and A549) increased the activities of caspase-3 and -7, but there were no significant increases in the activities of caspase-3 and -7 in the non-tumorigenic HEK293 cells with Mstn knockdown (Fig. S3).

To assess whether these alterations can be reversed by addition of recombinant Mstn to the culture medium of Mstn KO cells, we purified recombinant Mstn protein [28] (Fig. 4G) and verified the effect in HeLa and Mstn-deficient cells. As shown in Fig. 4H, we observed that prolonged exposure of Mstn caused significant viability loss of the HeLa cells in a dose-dependent manner. Nevertheless, the growth inhibition of HeLa/Mstn KO cells was reversed by addition of recombinant Mstn. On the dose, 300 ng/ml had achieved the best effect (Fig. 4I). In addition, adding culture media from normal HeLa cells also promoted HeLa/Mstn KO cell growth (Fig. 4J). The results suggest that the function of endogenous Mstn is indispensable for HeLa cell growth but exposure to exogenous Mstn at higher concentrations can be detrimental.

3.5. Mstn KO inhibited the tumor growth in the HeLa xenograft nude mice

We then determined whether the loss of Mstn induced HeLa cell apoptosis in a tumor xenograft model. The effect of Mstn KO on xenograft tumors was examined in immune-deficient nude mice. As shown in Figs. 5A and 5B, tumor progression was more rapid in the HeLa group than those inoculated with HeLa/Mstn KO cells. We also found that the tumor sizes in the Mstn KO group were significantly smaller than those in the HeLa group after injection for 22 days (Fig. 5C). The tumor weights were substantial reductions in mice bearing Mstn KO cells (Fig. 5D). We then tested whether the reduced tumor size was due to apoptosis, as observed in the cultured cancer cells. Indeed, TUNEL-staining analysis detected a markedly increased number of apoptotic tumor cells in the Mstn KO group compared with the HeLa group (60% vs. 4%) (Fig. 5E). We next examined whether adding Mstn promoted HeLa/Mstn KO cells growth in xenograft tumor models. When treated with Mstn, the growth inhibition of Mstn KO cells was obviously attenuated (Figs. 5F, 5G). Moreover, compared with the PBS group, the tumor weights in the Mstn treated group were significantly increased (Fig. 5H). These results demonstrate that the Mstn-deficiency can not only induce HeLa cell apoptosis *in vitro*, but also inhibits tumorigenesis *in vivo* in the xenograft tumor model.

3.6. Mstn KO triggered mitochondria-dependent apoptosis in HeLa cells

Mstn KO induced apparent changes in the morphology of mitochondria where they transformed from filamentous to dot-shaped (Fig. 6A). These dot-shaped mitochondria were also apparent in cells during apoptosis [29] or under metabolic stress-induced cell death [30]. To establish whether Mstn KO induces mitochondria- dependent apoptosis in HeLa cells, we measured the mitochondrial membrane potential using JC-1 dye staining. As shown in Fig. 6B, JC-1 aggregates accumulated in the mitochondrial membrane and emitted a strong red fluorescent signal in HeLa cells, thereby indicating no changes in the mitochondrial membrane potential. However, Mstn KO cells exhibited increased green fluorescence, which indicated the existence of monomeric JC-1 and depolarization of the mitochondrial membrane. Moreover, the significant decreases of fluorescence intensity due to TMRM (Fig. 6C) and rhodamine 123 (Fig. 6D) in the Mstn KO cells also reflected the loss of $\Delta\psi_m$. Following mitochondrial membrane depolarization, the redistribution of Cyt-c from mitochondria into the cytosol is a fundamental event during apoptosis, where Cyt-c activates caspases. Therefore, we investigated the cellular distribution of Cyt-c using immunostaining and subcellular fractionation assays. The presence of Cyt-c in the cytoplasm was confirmed by microscopy (Fig. 6E). Furthermore,

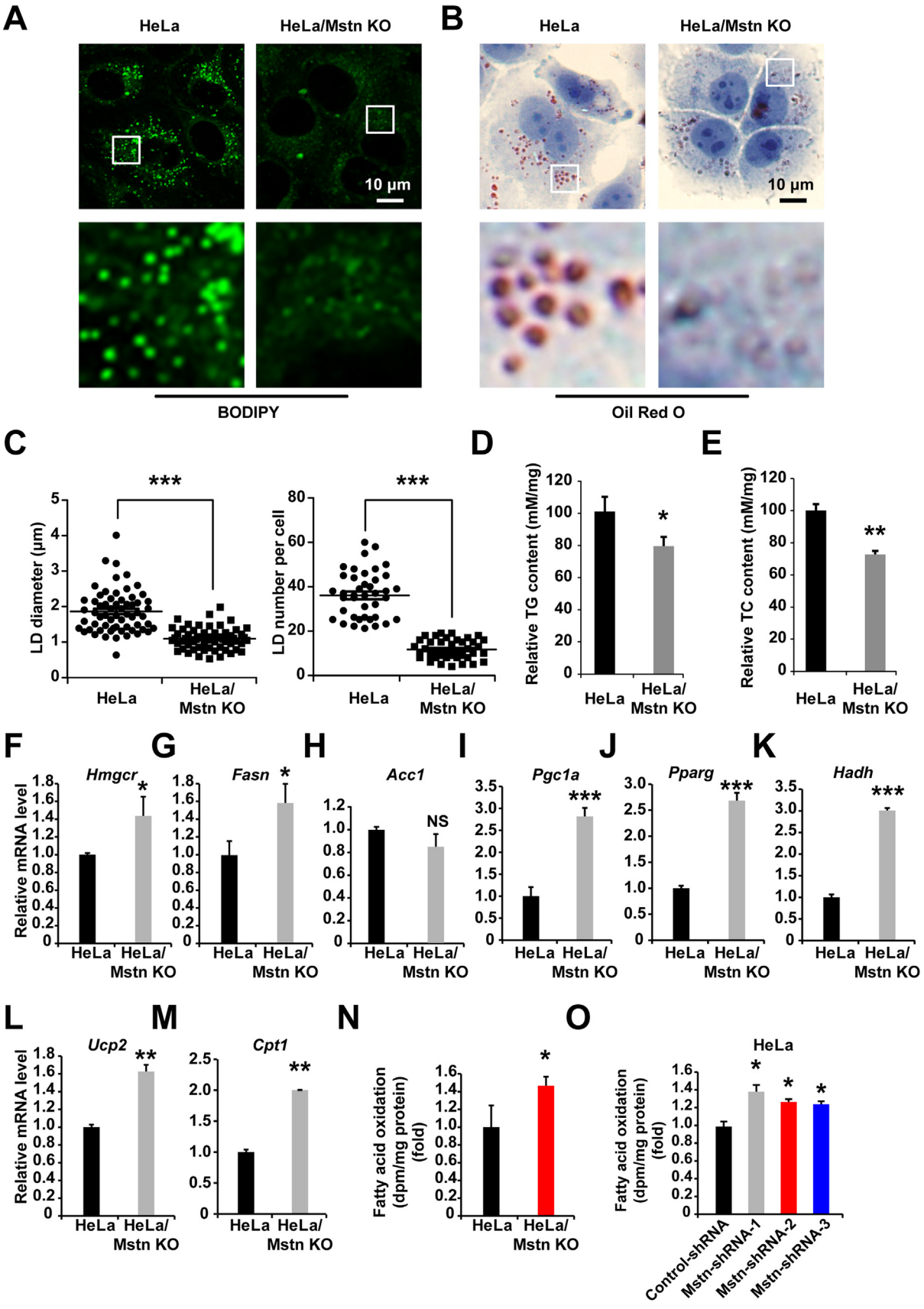

(caption on next page)

Fig. 7. Mstn KO reduced the lipid content and increased fatty acid oxidation. (A) LDs in cells were stained with BODIPY 493/503. The boxed region in the top image is enlarged on the bottom. Each image is representative of three independent experiments. (B) Cells were fixed and stained with Oil Red O. Nuclei were counterstained with hematoxylin. Scale bar, 10 μm. The boxed region in the top image is enlarged on the bottom. Each image is representative of three independent experiments. (C) Plots of the average LD diameter (left) and LD number per cell (right) in Oil Red O images are shown. At least 40 cells were counted. Data represent the mean ± standard error of the mean. $^{***}P < 0.0001$, unpaired two-tailed *t*-test. (D) TG concentrations in cells were normalized versus the cellular protein content. Data represent the mean ± standard error of the mean based on three independent experiments. $^{*}P < 0.05$, unpaired two-tailed *t*-test. (E) TC concentrations in cells were normalized versus the cellular protein content. Data represent the mean ± standard error of the mean based on three independent experiments. $^{**}P < 0.01$, unpaired two-tailed *t*-test. (F–M) The mRNA levels of *Hmgcr*, *Fasn*, *Acc1*, *Pgc1a*, *Pparg*, *Hadh*, *Ucp2*, and *Cpt1* were examined by Q-PCR in HeLa and HeLa/Mstn KO cells. Values were normalized relative to the *β-Actin* mRNA levels. Data represent the mean ± standard error of the mean based on three independent experiments. NS, not significant, $^{*}P < 0.05$, $^{**}P < 0.01$, $^{***}P < 0.0001$; unpaired two-tailed *t*-test. (N) Fatty acid oxidation in cells was determined as release of $^{3}H_2O$ from labeled palmitate. Data represent the mean ± standard error of the mean based on three independent experiments. $^{*}P < 0.05$; unpaired two-tailed *t*-test. (O) Fatty acid oxidation in control-shRNA or Mstn-shRNAs stably expressing HeLa cells was determined as release of $^{3}H_2O$ from labeled palmitate. Data represent the mean ± standard error of the mean based on three independent experiments. $^{*}P < 0.05$; unpaired two-tailed *t*-test.

subcellular fractionation and western blot analysis indicated that the levels of Cyt-c protein were significantly increased in the cytoplasmic fractions from Mstn KO cells compared with those from HeLa cells (Fig. 6F). In sum, these results demonstrate that mitochondria are involved in Mstn-deficiency induced HeLa cell apoptosis.

3.7. Mstn KO reduced the lipid content and activated fatty acid oxidation

Mstn inhibition leads to reduced body fat levels [31]. To investigate whether Mstn could affect fatty acid metabolism in cultured cancer cells, we examined the intracellular triglyceride (TG) and lipid contents by BODIPY493/503 and Oil Red O staining. Using microscopy, we observed reductions in the intensity of LDs in the cytoplasm of Mstn KO cells (Figs. 7A, 7B). LD diameter was decreased ~55% ($P < 0.0001$) compared to HeLa cells, while a ~67% ($P < 0.0001$) reduction in LD number (Fig. 7C). The total TG (Fig. 7D) and total cholesterol (TC) (Fig. 7E) contents were also lower compared with the control cells. We hypothesized that this could have been caused by reduced triglyceride synthesis or enhanced fatty acid oxidation. Subsequent Q-PCR analysis indicated the elevated expression of genes encoding enzymes involved with cholesterol synthesis (*Hmgcr*) (Fig. 7F) and fatty acid synthesis (*Fasn*) (Fig. 7G). However, the mRNA level of *Acc1*, another gene required for the biosynthesis of fatty acids, was not altered (Fig. 7H). Therefore, we considered that Mstn KO reduced the lipid contents due to increased energy expenditure. Consistent with this hypothesis, the mRNA levels of *Pgc1a* and *Pparg* were upregulated by several times, which are key transcriptional regulators of energy homeostasis, and there were corresponding increases in fatty acid oxidation (Figs. 7I, 7J). Furthermore, the HADH, UCP2, and CPT1 enzymes are correlated with fatty acid oxidation. We found that the *Hadh*, *Ucp2*, and *Cpt1* mRNA expression levels were markedly increased in HeLa/Mstn KO cells (Figs. 7K–7M). To correlate the increase in mRNA expression of fatty acid oxidation genes caused by Mstn with changes in lipid metabolism, we determined the rate of fatty acid oxidation in HeLa and KO cells. The oxidation of exogenously administered 9,10-[^{3}H]palmitate, measured by $^{3}H_2O$ production, increased 1.4-fold ($P < 0.05$) in Mstn KO cells compared with control group (Fig. 7N). In addition, the rate of fatty acid oxidation was also significantly increased in the Mstn-shRNAs stably expressing HeLa cells (Fig. 7O). These results indicate that the expression levels of key enzymes are upregulated by Mstn-deficiency, thereby enhancing fatty acid oxidation.

3.8. ROS generation involved in apoptosis of HeLa/Mstn KO cells

Tumor cells possess a high rate of glycolysis even in the presence of oxygen and fully functioning mitochondria. This process is known as the Warburg effect, it can protect cells from oxidative stress [12,16,17,32]. Our results demonstrate that mitochondria are involved in the Mstn KO-induced apoptosis of HeLa cells and that the levels of fatty acid oxidation are increased. To test whether fatty acid oxidation leads to ROS generation in cancer cells, we added the intracellular ROS sensors DCFH-DA or DHE to cells. As indicated in Figs. 8A and 8B, the generation of ROS was detected in Mstn KO cells by fluorescent microscopy ($P < 0.0001$). Moreover, after adding mitoPY1 (a mitochondria-specific fluorescent probe for H_2O_2) to the cell suspension, the intensity of green fluorescence significantly increased in the Mstn KO cells compared with the control group (Fig. 8C). In addition, the increased ROS production was confirmed in human cancer cells (Huh-7, HeLa, HepG2, and A549) expressing Mstn-shRNAs, while the non-tumorigenic HEK293 cells with Mstn knockdown had raised ROS levels but the increases were not significant (Fig. S4). These results demonstrate that the loss of Mstn triggers ROS generation. Strikingly, ROS production was markedly blocked by NAC or PEG-SOD treatment, but not by the NADPH oxidase inhibitor apocynin (Fig. 8D), thereby suggesting that the mitochondria-derived ROS but not NADPH oxidase was responsible for the accelerated generation of cellular ROS in Mstn KO cells. The free radical scavenging properties of NAC or PEG-SOD can be exploited as antioxidants. Thus, as expected, compared with the vehicle control and apocynin treatment, Mstn KO-induced apoptosis was partially abolished by NAC or PEG-SOD treatment (Figs. 8E–8G).

To explore whether ROS generation from enhanced fatty acid oxidation is the cause of Mstn KO cell apoptosis. Etomoxir, an inhibitor of carnitine palmi- toyltransferase 1 (CPT1) that blocks the rate-limiting step in fatty acid oxidation was used. First, the cytotoxic activity of etomoxir to HeLa cells was analyzed. Cells treated with 20 μm etomoxir, no significant reduction in cell viability was detected (Fig. S5A) and this concentration could significantly inhibit the rate of fatty acid oxidation (Fig. S5B). To confirm ROS generation was upstream or downstream of fatty acid oxidation in mitochondria, we evaluated the intracellular ROS level. As shown in Fig. 8H, intracellular ROS level in HeLa/Mstn KO cells was enhanced, whereas etomoxir significantly inhibited the increase of ROS generation. Furthermore, compared with the vehicle control treatment, the cell viability in Mstn KO cells was increased when fatty acid oxidation inhibited by etomoxir (Fig. 8I). In sum, ROS derived from enhanced fatty acid oxidation are involved in HeLa/Mstn KO cell apoptosis.

3.9. Model of Mstn KO induced ROS-mediated apoptosis in cancer cells

In summary, our results indicated that Mstn deficiency induced apoptosis in cancer cells. Mstn KO enhanced the fatty acid oxidation and reduced the cellular TG and TC contents, which ultimately triggered ROS generation. The increased production of ROS caused changes in the morphology, function, and physiology of mitochondria. These changes were followed by the release of Cyt-c into the cytoplasm, thereby causing caspase activation, and finally leading to mitochondria-dependent apoptosis in cancer cells (Fig. 9).

4. Discussion

Muscle loss and cachexia have been postulated to be key determinants of cancer-related death. Mstn is the negative regulator of muscle growth and a crucial player in the development of cancer cachexia [7]. However, the roles of Mstn in cancer as well as in regulating the

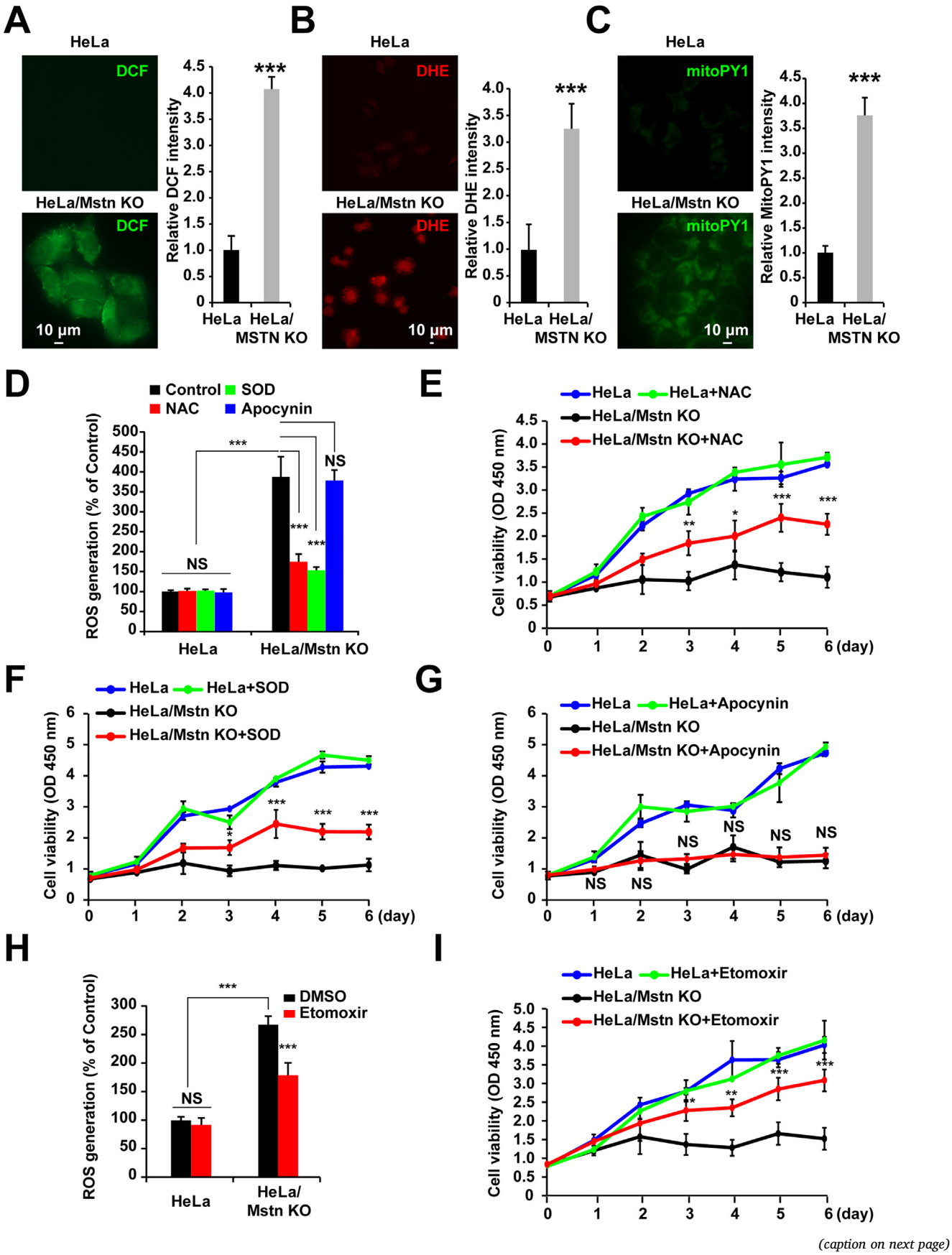

(caption on next page)

Fig. 8. ROS production in Mstn KO cells. (A) Cells were treated with 10 μM DCFH-DA for 30 min and fluorescence was detected using a fluorescence microscope. Scale bar, 10 μm. Image J analysis was used for semi-quantification of the fluorescence intensity. At least 300 cells were analyzed based on three independent experiments. Data represent the mean ± standard error of the mean. $^{***}P < 0.0001$, unpaired two-tailed *t*-test. (B) Cells were treated with 5 μM DHE for 30 min and fluorescence was detected using a fluorescence microscope. Scale bar, 10 μm. Image J analysis was used for semi-quantification of the fluorescence intensity. At least 300 cells were analyzed based on three independent experiments. Data represent the mean ± standard error of the mean. $^{***}P < 0.0001$, unpaired two-tailed *t*-test. (C) Cells were treated with 5 μM MitoPY1 for 30 min and fluorescence was detected using a fluorescence microscope. Scale bar, 10 μm. Image J analysis was used for semi-quantification of the fluorescence intensity. At least 300 cells were analyzed based on three independent experiments. Data represent the mean ± standard error of the mean. $^{***}P < 0.0001$, unpaired two-tailed *t*-test. (D) ROS production was measured using DCFH-DA. HeLa and HeLa/Mstn KO cells were incubated in the absence or presence of 1 mM NAC, PEG-SOD (150 U/ml), or 100 μM apocynin overnight. The fluorescent intensities of DCF were examined using a fluorescent plate reader. Data represent the mean ± standard error of the mean based on three independent experiments, which were analyzed by one-way ANOVA. NS, not significant, $^{***}P < 0.0001$. (E) Cell proliferation was analyzed using the CCK8 assay after incubation in the absence or presence of 300 μM NAC for the indicated time periods. Data represent the mean ± standard error of the mean based on three independent experiments, which were analyzed by one-way ANOVA. $^{*}P < 0.05$, $^{**}P < 0.01$, $^{***}P < 0.0001$. (F) Cell proliferation was analyzed using the CCK8 assay after incubation in the absence or presence of PEG-SOD (150 U/ml) for the indicated time periods. Data represent the mean ± standard error of the mean based on three independent experiments, which were analyzed by one-way ANOVA. $^{*}P < 0.05$, $^{***}P < 0.0001$. (G) Cell proliferation was analyzed using the CCK8 assay after incubation in the absence or presence of 100 μM apocynin for the indicated time periods. Data represent the mean ± standard error of the mean based on three independent experiments, which were analyzed by one-way ANOVA. NS, not significant. (H) ROS production was measured using DCFH-DA. HeLa and HeLa/Mstn KO cells were incubated in the absence or presence of 20 μM etomoxir for 48 h. The fluorescent intensities of DCF were examined using a fluorescent plate reader. Data represent the mean ± standard error of the mean based on three independent experiments, which were analyzed by one-way ANOVA. NS, not significant, $^{***}P < 0.0001$. (I) Cell proliferation was analyzed using the CCK8 assay after incubation in the absence or presence of 20 μM etomoxir for the indicated time periods. Data represent the mean ± standard error of the mean based on three independent experiments, which were analyzed by one-way ANOVA. $^{*}P < 0.05$, $^{**}P < 0.01$, $^{***}P < 0.0001$.

survival and growth of cancer cells remain obscure. In our study, the expression of Mstn in several types of tumor tissues was investigated, and consistent results had been confirmed. Immunofluorescent analysis of tissues from 10 gastric cancer patients , 10 lung cancer patients and 10 esophagus cancer patients demonstrated that cancer cells showed significantly staining of Mstn when compared to their corresponding pericarcinous tissues with positive nuclear staining (Fig. 1). We also found a capsule like structure contained a large number of Mstn (Figs. 1A3, 1B5, 1C3, 1C4, 1C6), these packages of Mstn in the capsule may also be released. As shown in Figs. 1A4, 1B3, 1B4, 1C3 and 1C6, Mstn proteins were dispersed in cancer tissues, if these Mstn circulates in the blood will lead to cachexia. In addition, we demonstrated that Mstn was expressed at higher levels in different types of human cancer cells compared with non-tumorigenic HEK293 cells (Fig. 2). We propose that Mstn is a cancer-related factor synthesized by cancer cells and that it induces severe skeletal muscle wasting during cancer cachexia. This hypothesis is consistent with the appearance of Mstn in the secretome of the murine C26 colon cancer model [33]. Furthermore, an early study detected the upregulation of Mstn signaling during the pathogenesis of muscle wasting in experimental cancer cachexia [3]. Similarly, elevated serum Mstn levels are correlated with muscle mass loss in patients with liver cirrhosis [34]. Thus, the inhibition of Mstn is a promising approach for treating cancer cachexia. Indeed, recent studies have shown that a therapeutic strategy based on blocking the Mstn pathway fully reverses skeletal muscle loss and dramatically prolongs the survival of tumor-bearing animals. However, the tumor growth rate and weight in the animals were not affected when Mstn pathway abolished by sActRIIB [7]. We consider the failure to decrease tumor growth rate and weight in mice, possibly because previous researchers utilized the intramuscular injection of ActRIIB's soluble extracellular domain, which inhibits receptor binding and the biological activity of Mstn, while the expression and function of Mstn within tumor were not affected. Therefore, inhibiting the synthesis and secretion of Mstn might be the most fundamental strategy for overcoming Mstn-related muscle wasting during cancer cachexia.

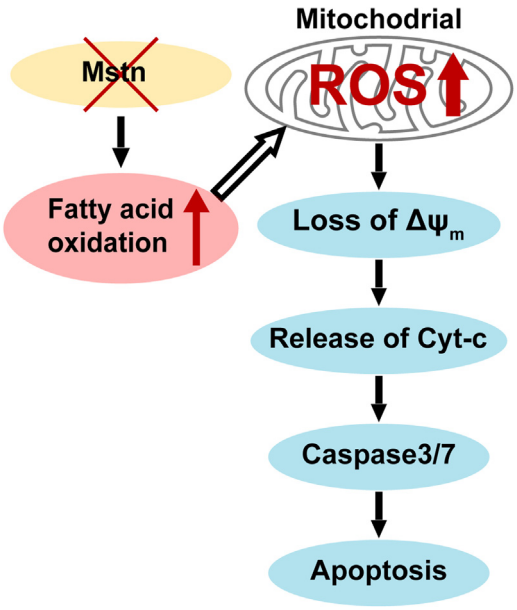

Fig. 9. Model of Mstn KO induced ROS-mediated apoptosis in cancer cells.

In the current study, we first found that lentivirus-mediated Mstn knockdown inhibited the growth and promoted the apoptosis of cancer cells (Huh7, HeLa, HepG2, and A549), but it had little effect on non-tumorigenic HEK293 cells (Fig. 2 and S3). To further confirm the correlation between Mstn level and cancer cell apoptosis, CRISPR/Cas9 was used to directly knock out Mstn in HeLa cells (which had the highest Mstn level). Our results demonstrated that Mstn KO not only induced apoptosis in HeLa cells *in vitro* (Fig. 4), but also inhibited tumorigenesis *in vivo* in a xenograft tumor model (Fig. 5), thereby suggesting that Mstn is a cancer-related protein that induces muscle loss and associates with tumor progression. Consequently, Mstn may represent an attractive drug target. In addition, our results showed that when Mstn was knocked out, there were changes in the mitochondrial morphology and function, which led to mitochondria-dependent apoptosis (Fig. 6). This effect may also be relevant to the severe health problems and low survival rate caused by Mstn KO in animals [35,36]. To the best of our knowledge, the present findings are the first experimental evidence to demonstrate that the genetic ablation of Mstn induces mitochondria-dependent apoptosis in cancer cells. Interestingly, a previous study showed that prolonged exposure to Mstn also induced mitochondria-dependent apoptosis in cancer cells, but the mechanism was attributed to Mstn induced metabolic shift from oxidative phosphorylation (OXPHOS) to glycolysis in glucose-addicted cancer cells, then, these metabolic changes and ATP depletion were causally linked with VDAC1 upregulated, HKII downregulated and Bax translocation to the mitochondria and subsequent apoptosis in cancer cells. In our study, it was found that the Mstn deficiency resulted in an increase in fatty acid oxidation, which further induced the formation of ROS, when ROS accumulated beyond the ability of cell reduction, apoptosis occurred. These observations are consistent with the result that Mstn-null mice showed slightly higher level of respiration ratio

than their wild type littermates [29]. Furthermore, when we exposed HeLa cells to wide range of Mstn concentrations, results confirmed the findings of Liu et al. [29] that higher doses of Mstn led to HeLa cell apoptosis (Fig. 4H). Collectively, evidence has suggested Mstn plays an important role in regulating mitochondrial energy metabolism, too much or too little both can be bad to cancer cells. Thus, the function of Mstn is complicated, its role in modulating the balance between OXPHOS and glycolysis requires further investigation.

Previous studies demonstrated that $Mstn^{-/-}$ mice exhibited atrophied adipocytes and a failure to accumulate fat [37,38]. But the $Mstn^{-/-}$ mice are normal animals, the differences between cancer cells and normal cells are vast. We tried to assess whether loss of Mstn could affect fatty acid metabolism in cultured cancer cells. As shown in Fig. 7, TC and TG contents were strongly reduced in these KO cells. We hypothesized that this could have been due to reduced triacylglycerol synthesis or enhanced fatty acid oxidation. Q-PCR analysis indicated the upregulation of fatty acid oxidation- related genes, while the expression levels of genes involved with triglyceride or cholesterol synthesis were increased or unchanged. The rate of labeled fatty acid oxidation was also increased (Fig. 7). In addition, two previous studies confirmed an increase in the total energy expenditure in $Mstn^{-/-}$ mice [10,39], which suggests that increased fatty acid oxidation could be a key factor related to the reduced lipid composition in Mstn KO cells. We also hypothesized that Mstn KO could increase the activity of AMP-activated protein kinase (AMPK), which is a critical regulator of energy metabolism and the expression of genes involved with fatty acid oxidation [40]. Furthermore, AMPK activation has been shown to increase fatty acid oxidation [41]. Consistent with this finding, our unpublished results confirmed the increased phosphorylation of AMPKα in Mstn KO cells. Besides, it has been shown that the activation of ActRIIB by Mstn inhibits the phosphorylation of Akt, which is a key activator of the mTOR pathway related to protein synthesis and an inhibitor of FoxO1, which promotes protein degradation [42]. Thus, Mstn KO should increase protein synthesis and decrease protein degradation to increase the overall levels of proteins, including AMPK and fatty acid oxidation-related enzymes. Finally, Akt stimulates aerobic glycolysis in cancer cells and when the ATP levels are decreased, the compensatory responses of cells may enhance the oxidation of fatty acid to supply sufficient energy for cell survival [29,43]. The known Mstn signaling is initiated by mature Mstn binding first to ActRIIB receptor. However, the potential role of precursor Mstn that binds to DNA or interacts with other regulatory factors to govern gene expression is still largely unknown. Much attention should focus on the mechanisms changed by Mstn deficiency within cancer cells.

Cancer cells are characterized by a high rate of glycolysis, which is associated with a lower pyruvate oxidation rate. In general, cancer cells are more active in terms of the production of ROS than normal cells, and they are under intrinsic oxidative stress due to their increased metabolic stress and proliferative capacity, and thus they are more sensitive to oxidative stress [35]. Limited mitochondrial respiration and OXPHOS reduces oxidative stress during DNA replication and in phases of high biosynthetic activity [12,16,17,44]. Increased fatty acid oxidation occurs in mitochondria and it is associated with increased OXPHOS and net ROS production [45]. SOD enzymes are key antioxidant enzymes involved with the metabolic elimination of ROS, and our Q-PCR analyses showed that the expression levels of SOD1 and SOD2 were generally higher in cancer cells compared with HEK293 cells (Fig. S6). The increased expression levels of SOD1 and SOD2 in cancer cells reflect the cellular response to intrinsic oxidative stress, and their upregulation may be an important adaptation mechanism that provides more sustainable protection against increased ROS stress. However, this adaptation process appears to have a limited capacity in cancer cells, where ROS stress is enhanced further to a point that triggers cell death. In the current study, increased ROS production was obtained in HeLa/Mstn KO cells (Figs. 8A–8D) and human cancer cells (Huh-7, HeLa, HepG2, and A549) via the lentivirus-mediated RNAi of Mstn, while the non-tumorigenic HEK293 cells with Mstn knockdown had raised ROS levels but the increase was not significant (Fig. S4). The administration of ROS scavengers prevented the accumulation of ROS and abrogated apoptosis (Figs. 8D–8F). In Mstn KO groups treated with etomoxir, ROS level was attenuated and cell viability was significantly improved (Figs. 8H, 8I), indicating that fatty acid oxidation and ROS were involved in the reduction of cell proliferation. Overall, these results indicate that ROS accumulation is a necessary and critical event in the loss-of-Mstn-induced apoptosis in cancer cells.

It should be noted that only a slight increase in cellular ROS was observed in non-tumorigenic HEK293 cells with Mstn knockdown (Fig. S4). It is likely that when normal cells are under oxidative stress, they can downregulate their mitochondrial respiratory activity so less ROS are generated in the cells. Previous studies detected a 30% decrease in oxygen consumption (an indication of mitochondrial respiratory activity) when normal lymphocytes were incubated with ROS-generating agents. However, this downregulation of mitochondrial respiration was absent in cancer cells and they continued to consume high levels of oxygen when incubated with ROS-generating agents under the same conditions [35]. Thus, the ability of normal cells to downregulate their oxidative activity when exposed to ROS stress may be a mechanism that protects cells from further ROS production, and thus oxidative damage. This is consistent with our observation that the knockdown of Mstn did not induce apparent changes in the mitochondrial morphology of HEK293 cells, and the rate of fatty acid oxidation was also not altered (Fig. S7). The molecular basis of the downregulation of the mitochondrial respiration in response to oxidative stress in normal cells is not clear at present, and it is an important subject of future investigations.

Our study demonstrated that it may be possible to exploit the novel function of Mstn in regulating mitochondrial metabolism and apoptosis within cancer cells. The therapeutic disruption of Mstn expression in cancer cells may be a logical strategy for inhibiting cancer growth and muscle loss during cachexia. Further evaluations of this possible therapeutic strategy in preclinical and clinical settings are warranted.

5. Conclusions

We found that Mstn was expressed at higher levels in different types of human tumor tissues and cancer cells, it played an important role in regulating the survival and growth of cancer cells. Given the influential functions of Mstn, we suggest that loss of Mstn could be a useful tool for fighting cancer and muscle loss during cancer cachexia due to enhanced fatty acid oxidation and ROS-induced apoptosis. Agents that target fatty acid oxidation or ROS generation will probably need to be combined with sActRIIB or anti-Mstn antibodies to successfully overcome muscle loss during cancer cachexia. The intra-tumoral injection or virus-mediated treatment with Cas9 as well as a sgRNA against Mstn may be an effective method for combating cancer while avoiding the deteriorating effects on muscle. Further studies, especially *in vivo* studies, are now required to assess whether similar effects to those observed *in vitro* also occur in solid tumors.

Acknowledgments

This study was supported by a grant for Outstanding Talents of Henan Agricultural University (30600773) and the Ministry of Agriculture of China (2016ZX08006001-006).

Conflicts of interests' statement

We declare that we have no potential conflicts of interests concerning this work.

Appendix A. Supporting information

Supplementary data associated with this article can be found in the online version at doi:10.1016/j.redox.2018.09.009.

References

[1] A.C. Durieux, A. Amirouche, S. Banzet, N. Koulmann, R. Bonnefoy, M. Pasdeloup, C. Mouret, X. Bigard, A. Peinnequin, D. Freyssenet, Ectopic expression of myostatin induces atrophy of adult skeletal muscle by decreasing muscle gene expression, Endocrinology 148 (7) (2007) 3140–3147.

[2] T.A. Zimmers, M.V. Davies, L.G. Koniaris, P. Haynes, A.F. Esquela, K.N. Tomkinson, A.C. McPherron, N.M. Wolfman, S.J. Lee, Induction of cachexia in mice by systemically administered myostatin, Science 296 (5572) (2002) 1486–1488.

[3] P. Costelli, M. Muscaritoli, A. Bonetto, F. Penna, P. Reffo, M. Bossola, G. Bonelli, G.B. Doglietto, F.M. Baccino, F. Rossi Fanelli, Muscle myostatin signalling is enhanced in experimental cancer cachexia, Eur. J. Clin. Investig. 38 (7) (2008) 531–538.

[4] K. Harada, Y. Shintani, Y. Sakamoto, M. Wakatsuki, K. Shitsukawa, S. Saito, Serum immunoreactive activin A levels in normal subjects and patients with various diseases, J. Clin. Endocrinol. Metab. 81 (6) (1996) 2125–2130.

[5] S. Wildi, J. Kleeff, H. Maruyama, C.A. Maurer, M.W. Buchler, M. Korc, Overexpression of activin A in stage IV colorectal cancer, Gut 49 (3) (2001) 409–417.

[6] K.T. Murphy, A. Chee, B.G. Gleeson, T. Naim, K. Swiderski, R. Koopman, G.S. Lynch, Antibody-directed myostatin inhibition enhances muscle mass and function in tumor-bearing mice, Am. J. Physiol. Regul. Integr. Comp. Physiol. 301 (3) (2011) R716–R726.

[7] X. Zhou, J.L. Wang, J. Lu, Y. Song, K.S. Kwak, Q. Jiao, R. Rosenfeld, Q. Chen, T. Boone, W.S. Simonet, D.L. Lacey, A.L. Goldberg, H.Q. Han, Reversal of cancer cachexia and muscle wasting by ActRIIB antagonism leads to prolonged survival, Cell 142 (4) (2010) 531–543.

[8] A.C. McPherron, S.J. Lee, Suppression of body fat accumulation in myostatin-deficient mice, J. Clin. Investig. 109 (5) (2002) 595–601.

[9] K. Burgess, T. Xu, R. Brown, B. Han, S. Welle, Effect of myostatin depletion on weight gain, hyperglycemia, and hepatic steatosis during five months of high-fat feeding in mice, PLoS One 6 (2) (2011) e17090.

[10] S.J. Choi, Z. Yablonka-Reuveni, K.J. Kaiyala, K. Ogimoto, M.W. Schwartz, B.E. Wisse, Increased energy expenditure and leptin sensitivity account for low fat mass in myostatin-deficient mice, Am. J. Physiol. Endocrinol. Metab. 300 (6) (2011) E1031–E1037.

[11] R.K. Ockner, R.M. Kaikaus, N.M. Bass, Fatty-acid metabolism and the pathogenesis of hepatocellular carcinoma: review and hypothesis, Hepatology 18 (3) (1993) 669–676.

[12] G. Peluso, R. Nicolai, E. Reda, P. Benatti, A. Barbarisi, M. Calvani, Cancer and anticancer therapy-induced modifications on metabolism mediated by carnitine system, J. Cell. Physiol. 182 (3) (2000) 339–350.

[13] C. Prip-Buus, A.C. Bouthillier-Voisin, C. Kohl, F. Demaugre, J. Girard, J.P. Pegorier, Evidence for an impaired long-chain fatty acid oxidation and ketogenesis in Fao hepatoma cells, Eur. J. Biochem. 209 (1) (1992) 291–298.

[14] P.T. Schumacker, Reactive oxygen species in cancer cells: live by the sword, die by the sword, Cancer Cell 10 (3) (2006) 175–176.

[15] G. Waris, H. Ahsan, Reactive oxygen species: role in the development of cancer and various chronic conditions, J. Carcinog. 5 (2006) 14.

[16] K.A. Brand, U. Hermfisse, Aerobic glycolysis by proliferating cells: a protective strategy against reactive oxygen species, FASEB J. 11 (5) (1997) 388–395.

[17] U. Wenzel, A. Nickel, H. Daniel, Increased carnitine-dependent fatty acid uptake into mitochondria of human colon cancer cells induces apoptosis, J. Nutr. 135 (6) (2005) 1510–1514.

[18] B. Kalyanaraman, V. Darley-Usmar, K.J. Davies, P.A. Dennery, H.J. Forman, M.B. Grisham, G.E. Mann, K. Moore, L.J. Roberts 2nd, H. Ischiropoulos, Measuring reactive oxygen and nitrogen species with fluorescent probes: challenges and limitations, Free Radic. Biol. Med. 52 (1) (2012) 1–6.

[19] D.C. Fernandes, J. Wosniak Jr., L.A. Pescatore, M.A. Bertoline, M. Liberman, F.R. Laurindo, C.X. Santos, Analysis of DHE-derived oxidation products by HPLC in the assessment of superoxide production and NADPH oxidase activity in vascular systems, Am. J. Physiol. Cell Physiol. 292 (1) (2007) C413–C422.

[20] B.C. Dickinson, V.S. Lin, C.J. Chang, Preparation and use of MitoPY1 for imaging hydrogen peroxide in mitochondria of live cells, Nat. Protoc. 8 (6) (2013) 1249–1259.

[21] I. De Proost, I. Pintelon, I. Brouns, A.B. Kroese, D. Riccardi, P.J. Kemp, J.P. Timmermans, D. Adriaensen, Functional live cell imaging of the pulmonary neuroepithelial body microenvironment, Am. J. Respir. Cell Mol. Biol. 39 (2) (2008) 180–189.

[22] D.C. Joshi, J.C. Bakowska, Determination of mitochondrial membrane potential and reactive oxygen species in live rat cortical neurons, J. Vis. Exp.: JoVE 51 (2011).

[23] S.W. Perry, J.P. Norman, J. Barbieri, E.B. Brown, H.A. Gelbard, Mitochondrial membrane potential probes and the proton gradient: a practical usage guide, BioTechniques 50 (2) (2011) 98–115.

[24] A. Cabrero, M. Alegret, R.M. Sanchez, T. Adzet, J.C. Laguna, M. Vazquez, Bezafibrate reduces mRNA levels of adipocyte markers and increases fatty acid oxidation in primary culture of adipocytes, Diabetes 50 (8) (2001) 1883–1890.

[25] Y.S. Gallot, A.C. Durieux, J. Castells, M.M. Desgeorges, B. Vernus, L. Plantureux, D. Remond, V.E. Jahnke, E. Lefai, D. Dardevet, G. Nemoz, L. Schaeffer, A. Bonnieu, D.G. Freyssenet, Myostatin gene inactivation prevents skeletal muscle wasting in cancer, Cancer Res. 74 (24) (2014) 7344–7356.

[26] T. Hamid, M.T. Malik, S.S. Kakar, Ectopic expression of PTTG1/securin promotes tumorigenesis in human embryonic kidney cells, Mol. Cancer 4 (1) (2005) 3.

[27] C. Zhao, X. Wang, Y. Zhao, Z. Li, S. Lin, Y. Wei, H. Yang, A novel xenograft model in zebrafish for high-resolution investigating dynamics of neovascularization in tumors, PLoS One 6 (7) (2011) e21768.

[28] W. Yang, Y. Zhang, G. Ma, X. Zhao, Y. Chen, D. Zhu, Identification of gene expression modifications in myostatin-stimulated myoblasts, Biochem. Biophys. Res. Commun. 326 (3) (2005) 660–666.

[29] Y. Liu, H. Cheng, Y. Zhou, Y. Zhu, R. Bian, Y. Chen, C. Li, Q. Ma, Q. Zheng, Y. Zhang, H. Jin, X. Wang, Q. Chen, D. Zhu, Myostatin induces mitochondrial metabolic alteration and typical apoptosis in cancer cells, Cell Death Dis. 4 (2013) e494.

[30] X. Liu, G. Hajnoczky, Altered fusion dynamics underlie unique morphological changes in mitochondria during hypoxia-reoxygenation stress, Cell Death Differ. 18 (10) (2011) 1561–1572.

[31] B. Buehring, N. Binkley, Myostatin–the holy grail for muscle, bone, and fat? Curr. Osteoporos. Rep. 11 (4) (2013) 407–414.

[32] U. Wenzel, S. Kuntz, M.D. Brendel, H. Daniel, Dietary flavone is a potent apoptosis inducer in human colon carcinoma cells, Cancer Res. 60 (14) (2000) 3823–3831.

[33] S. Lokireddy, I.W. Wijesoma, S. Bonala, M. Wei, S.K. Sze, C. McFarlane, R. Kambadur, M. Sharma, Myostatin is a novel tumoral factor that induces cancer cachexia, Biochem. J. 446 (1) (2012) 23–36.

[34] H. Nishikawa, H. Enomoto, A. Ishii, Y. Iwata, Y. Miyamoto, N. Ishii, Y. Yuri, K. Hasegawa, C. Nakano, T. Nishimura, K. Yoh, N. Aizawa, Y. Sakai, N. Ikeda, T. Takashima, R. Takata, H. Iijima, S. Nishiguchi, Elevated serum myostatin level is associated with worse survival in patients with liver cirrhosis, J. Cachex. Sarcopenia Muscle 8 (6) (2017) 915–925.

[35] R. Guo, Y. Wan, D. Xu, L. Cui, M. Deng, G. Zhang, R. Jia, W. Zhou, Z. Wang, K. Deng, M. Huang, F. Wang, Y. Zhang, Generation and evaluation of Myostatin knock-out rabbits and goats using CRISPR/Cas9 system, Sci. Rep. 6 (2016) 29855.

[36] C. Proudfoot, D.F. Carlson, R. Huddart, C.R. Long, J.H. Pryor, T.J. King, S.G. Lillico, A.J. Mileham, D.G. McLaren, C.B. Whitelaw, S.C. Fahrenkrug, Genome edited sheep and cattle, Transgenic Res. 24 (1) (2015) 147–153.

[37] J. Lin, H.B. Arnold, M.A. Della-Fera, M.J. Azain, D.L. Hartzell, C.A. Baile, Myostatin knockout in mice increases myogenesis and decreases adipogenesis, Biochem. Biophys. Res. Commun. 291 (3) (2002) 701–706.

[38] C. Zhang, C. McFarlane, S. Lokireddy, S. Masuda, X. Ge, P.D. Gluckman, M. Sharma, R. Kambadur, Inhibition of myostatin protects against diet-induced obesity by enhancing fatty acid oxidation and promoting a brown adipose phenotype in mice, Diabetologia 55 (1) (2012) 183–193.

[39] B.L. Bernardo, T.S. Wachtmann, P.G. Cosgrove, M. Kuhn, A.C. Opsahl, K.M. Judkins, T.B. Freeman, J.R. Hadcock, N.K. LeBrasseur, Postnatal PPARdelta activation and myostatin inhibition exert distinct yet complimentary effects on the metabolic profile of obese insulin-resistant mice, PLoS One 5 (6) (2010) e11307.

[40] C. Zhang, C. McFarlane, S. Lokireddy, S. Bonala, X. Ge, S. Masuda, P.D. Gluckman, M. Sharma, R. Kambadur, Myostatin-deficient mice exhibit reduced insulin resistance through activating the AMP-activated protein kinase signalling pathway, Diabetologia 54 (6) (2011) 1491–1501.

[41] C. Canto, Z. Gerhart-Hines, J.N. Feige, M. Lagouge, L. Noriega, J.C. Milne, P.J. Elliott, P. Puigserver, J. Auwerx, AMPK regulates energy expenditure by modulating NAD+ metabolism and SIRT1 activity, Nature 458 (7241) (2009) 1056–1060.

[42] J.M. Argiles, M. Orpi, S. Busquets, F.J. Lopez-Soriano, Myostatin: more than just a regulator of muscle mass, Drug Discov. Today 17 (13–14) (2012) 702–709.

[43] R.L. Elstrom, D.E. Bauer, M. Buzzai, R. Karnauskas, M.H. Harris, D.R. Plas, H. Zhuang, R.M. Cinalli, A. Alavi, C.M. Rudin, C.B. Thompson, Akt stimulates aerobic glycolysis in cancer cells, Cancer Res. 64 (11) (2004) 3892–3899.

[44] U. Wenzel, K. Schoberl, K. Lohner, H. Daniel, Activation of mitochondrial lactate uptake by flavone induces apoptosis in human colon cancer cells, J. Cell. Physiol. 202 (2) (2005) 379–390.

[45] M.G. Rosca, E.J. Vazquez, Q. Chen, J. Kerner, T.S. Kern, C.L. Hoppel, Oxidation of fatty acids is the source of increased mitochondrial reactive oxygen species production in kidney cortical tubules in early diabetes, Diabetes 61 (8) (2012) 2074–2083.